Supplementary Information for

Wafer-Scale Single-Crystal Monolayer Graphene Grown Directly on Insulating Substrates

Junzhu Li[1,2], Mingguang Chen[1], Abdus Samad[1], Haocong Dong[1,2], Avijeet Ray[1], Junwei Zhang[3], Xiaochuan Jiang[2,4], Udo Schwingenschlögl[1], Bo Tian[1,2]*, Xixiang Zhang[1]*

[1]Physical Science and Engineering Division, King Abdullah University of Science and Technology (KAUST), Thuwal 23955-6900, Saudi Arabia.

[2]Eleven-dimensional Nanomaterial Research Institute, Xiamen 361005, China.

[3]Key Laboratory of Magnetism and Magnetic Materials of Ministry of Education, Lanzhou University, Lanzhou 730000, China.

[4]Department of Physics, Xiamen University, Xiamen 361005, China.

*e-mail: bo.tian@kaust.edu.sa; xixiang.zhang@kaust.edu.sa

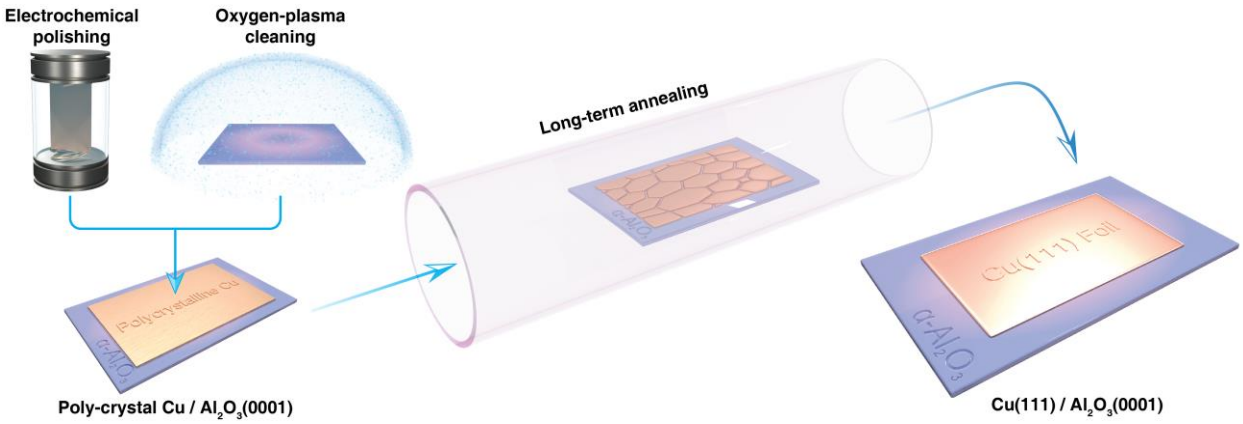

Fig. 1 | Schematic of the fabrication process of single-crystal Cu(111) foil from commercial polycrystalline Cu foil on Al_2O_3(0001). First, the as-received polycrystalline Cu foil was electrochemically polished. Meanwhile, the Al_2O_3(0001) was cleaned by the oxygen-plasma treatment. The Cu foil was then pressed onto the surface of Al_2O_3(0001). After that, this heterostructure was placed into the CVD system and further treated with long-term annealing under the condition of 1350 K, 750 Torr, 50-sccm H_2, and 50-sccm Ar. During the annealing process, under the thermal-energy disturbance at near-melting temperature, the other orientated crystals gradually relaxed and changed to the lowest stacking energy statues as Cu(111) crystals. As a result, the grain size and the components of the Cu(111) crystals continuously increased until they occupied the entire area.

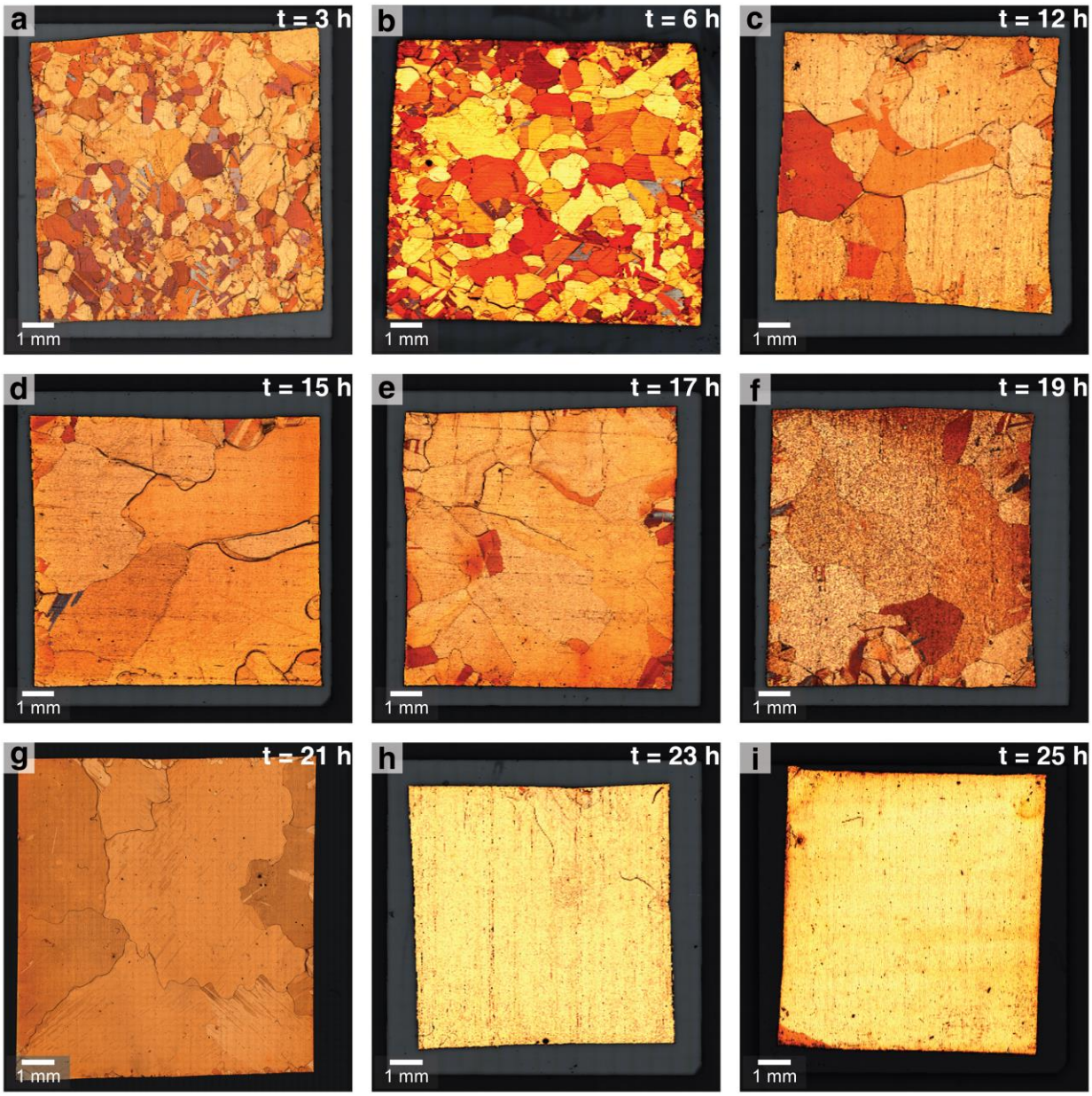

Fig. 2 | Optical micrograph of Cu foil surface (10×10 mm^2, after oxidization treatment) along various annealing times. a-i, Samples of different annealing times from 0 to 25 h under the specific condition of 1350 K, 750 Torr, 50-sccm H_2, and 50-sccm Ar. Since the color of CuO_x changes depending on crystal orientations, the phase transformation could be easily observed from optical images of oxidized Cu foil samples. The number of Cu grains gradually decreased along with the annealing time increase, and the size of the largest grain increased until it filled the entire area.

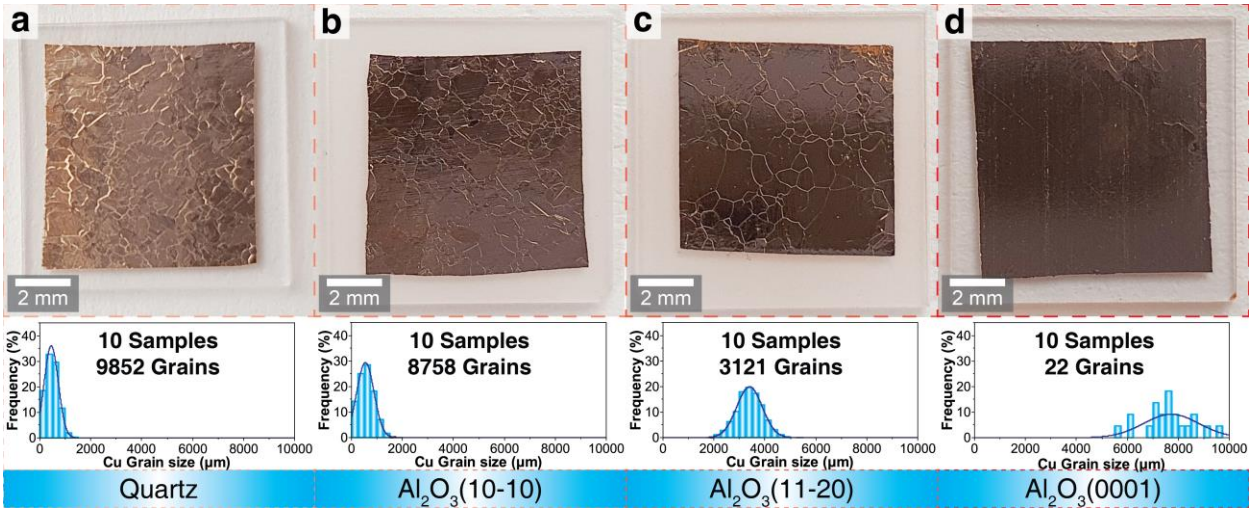

Fig. 3 | Photograph of Cu foil surface (10×10 mm^2, non-oxidization treatment) annealed along with various substrates. a, Quartz, **b**, m-plane Al_2O_3(10-10), **c,** a-plane Al_2O_3(11-20), **d,** c-plane Al_2O_3(0001). Corresponding Cu grain-size distributions were collected from 10 samples of each substrate. For comparison, the same annealing experimental condition of 1350 K, 750 Torr, 50-sccm H_2, and 50-sccm Ar were performed using various substrates for an annealing time of 20 h. From the results, except from the c-plane Al_2O_3(0001) substrate, none of the others exhibited phase transformations to single Cu(111), which is caused by the large lattice asymmetry and mismatch between the Cu(111) and the substrate crystals.

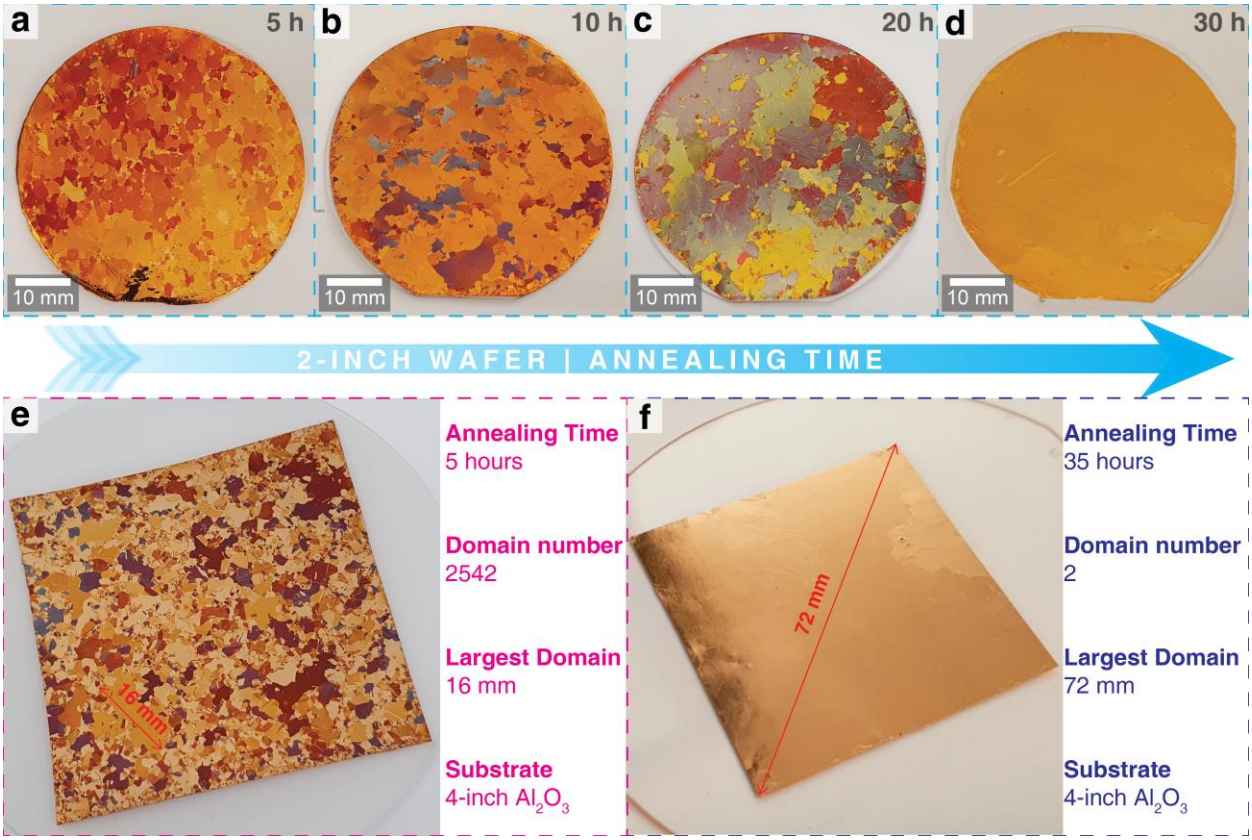

Fig. 4 | Photograph of produced large-scale Cu foil after oxidization treatment. a-d, Photograph of 2-inch Cu foil along various annealing times from 5 to 30 hours under the annealing condition of 1350 K, 750 Torr, 50-sccm H_2, and 50-sccm Ar. The color contrast indicates different Cu crystal grains. **e,** Cu foils annealed on a 4-inch Al_2O_3(0001) wafer for 5 hours with clearly-seen crystal grains. **f,** The Cu foil annealed for 35 hours on a 4-inch Al_2O_3(0001) wafer, which shows that the Cu(111) crystal almost occupies its entire area with the maximum diameter of 72 mm.

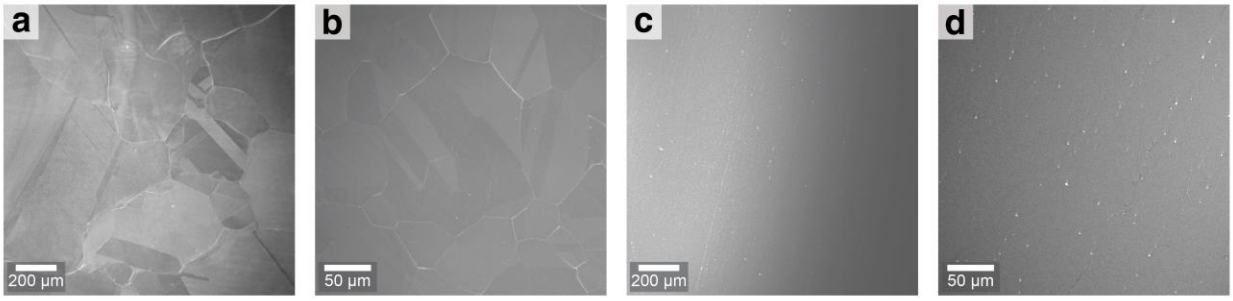

Fig. 5 | Surface morphology of fabricated Cu foil along with various annealing times. a-b, SEM images of Cu foil surface annealed for 5 hours. The grain boundaries are exhibited clearly as approximately hundred microns. **c-d,** SEM images of Cu foil annealed for 30 hours. Almost no grain boundary can be observed in the large view area. The annealing experiments were conducted in a 3-inch CVD system with the condition of 1350 K, 750 Torr, 50-sccm H_2, and 50-sccm Ar. (low magnification (left) and high magnification (right)).

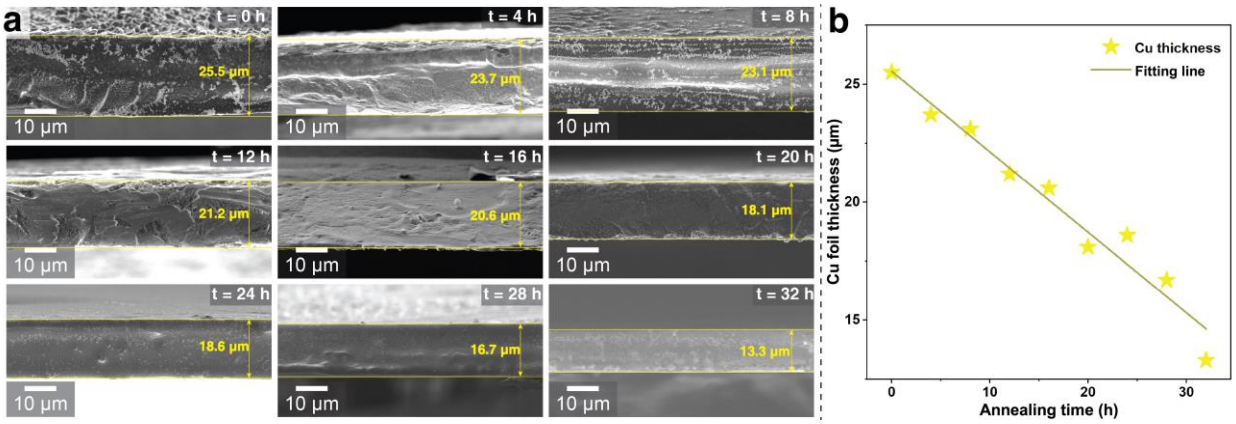

Fig. 6 | Thickness measurements of annealed Cu foils. a, Cross-section SEM images of annealed Cu foil for annealing time from 0 to 32 hours under the annealing conditions of 1350 K, 750 Torr, 50-sccm H_2, and 50-sccm Ar. **b,** Measured thickness of the center position of Cu foils versus annealing time. From the results, the thickness of Cu foil is decreased proportional to the annealing time, which means the Cu evaporated heavily during the annealing process. That is one of the reasons of why we choose the 25-μm Cu foil instead of the sputtered hundred-nanometer-thickness Cu film for the graphene growth experiments. To obtain a perfect interface state of the bottom surface of Cu and the extremely close distance between Cu(111) and Al_2O_3(0001), we need to select the thick enough Cu foil to avoid the complete evaporation during the annealing process.

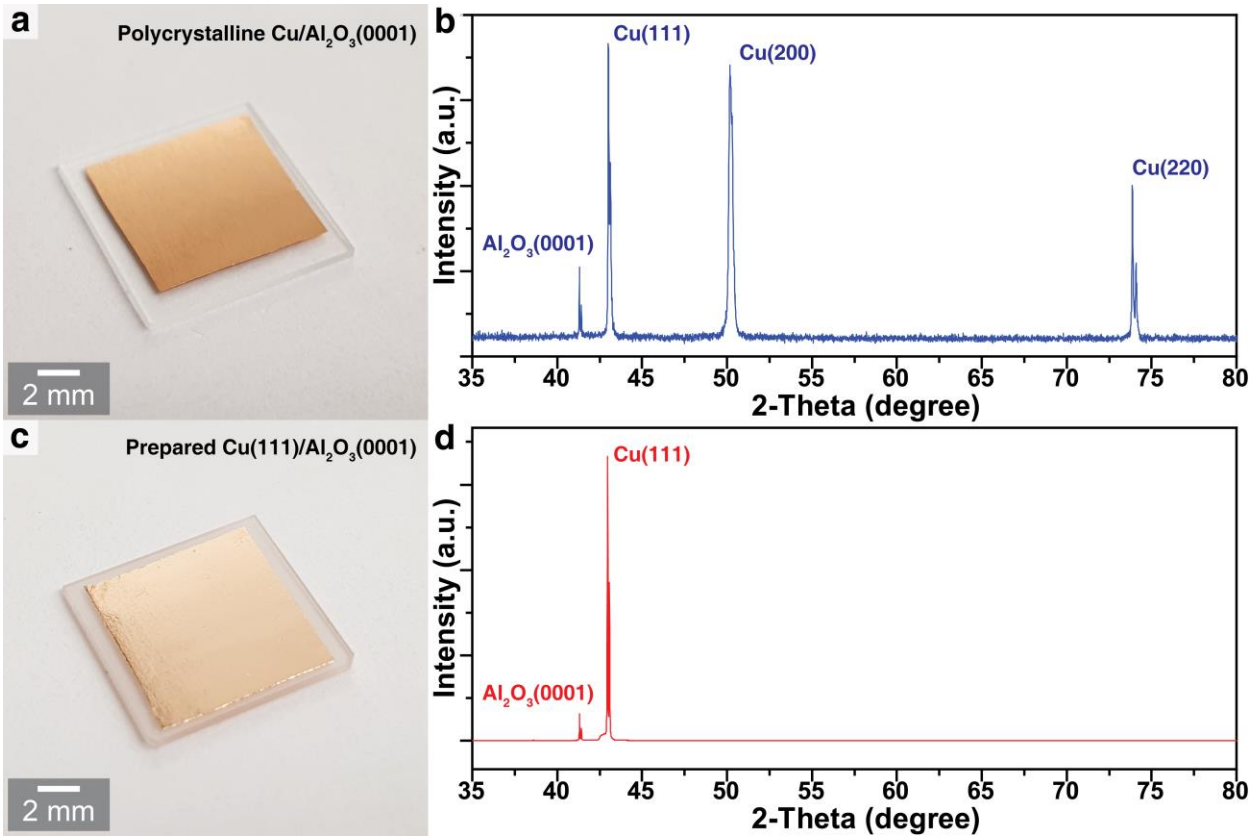

Fig. 7 | XRD characterization of non-annealed polycrystalline Cu and single-crystal Cu(111). a, Photograph of non-annealed polycrystalline Cu foil on Al_2O_3(0001) substrate. **b,** XRD spectra of polycrystalline Cu foil shown in (a). The Cu(111), Cu(200), and Cu(220) peak were distinctly observed in the spectra. **c,** Photograph of annealed polycrystalline Cu(111) foil on Al_2O_3(0001) substrate (annealing time: 30 h; annealing conditions: 1350 K, 750 Torr, 50-sccm H_2, and 50-sccm Ar). **d,** XRD spectra of annealed Cu(111) foil shown in (c). Only the sharp Cu(111) peak and the substrate peak can be observed in the spectra.

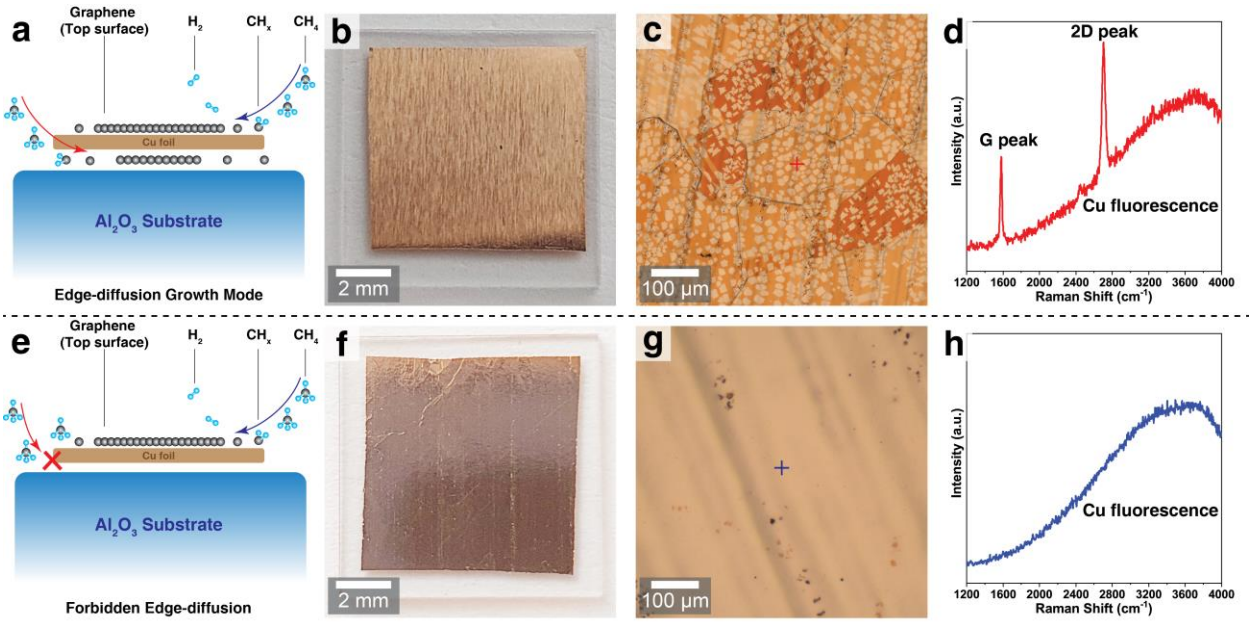

Fig. 8 | Compared fast CVD growth with unannealed Cu/Al_2O_3 and annealed Cu(111) /Al_2O_3. a, Schematic illustration of the graphene formation by edge-diffusion growth mode in CVD when the gap of Cu/Al_2O_3 is large. **b,** The photo of unannealed Cu/Al_2O_3 before graphene growth. **c,** The graphene formation in the back surface of Cu foil after peel off. **d,** The Raman signal of graphene detected from the position in (c). From the results, the graphene domains were formed with high nucleus density and small domain size. **e,** Schematic illustration of the methane entrance forbidden due to the extreme-small gap thinness between the annealed Cu(111) foil with Al_2O_3(0001) substrate. **f,** The photo of annealed Cu(111)/Al_2O_3 before graphene growth. **g,** No graphene can be observed in the back surface of the Cu(111) foil after peeling off. **h,** Only Cu fluorescence Raman signal can be detected in the area of (g).

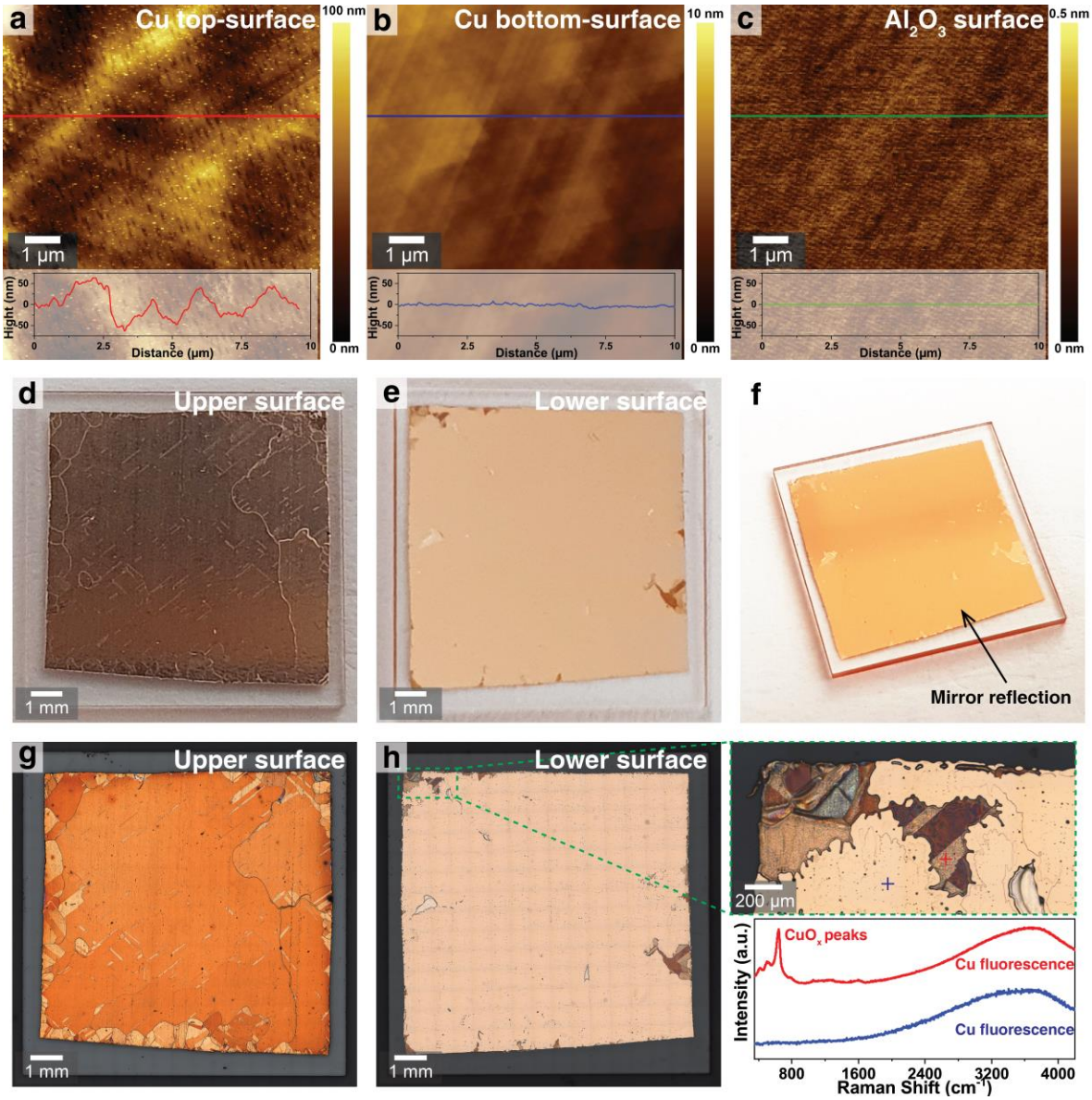

Fig. 9 | Surface roughness measurements of Cu foil. a-c, The AFM characterizations of the top surface of Cu foil (a), the bottom surface of Cu foil (b), and the surface of Al_2O_3(0001) substrate (c) after the long-term annealing process. The roughness is largest on the top surface of Cu foil, reaching 100 nm. The roughness of the bottom side is smaller, less than 10 nm, which is near the roughness of the Al_2O_3(0001) substrate, at 500 pm. The height profile figures were set to the same y-axis for comparisons. **d-f,** The photographs of annealed Cu/Al_2O_3(0001) sample. The top surface is rough, and the bottom surface is smoother. From the image in (f), a mirror-like surface can be seen from the backside of the Al_2O_3(0001) substrate, which means the bottom surface has a very smooth surface and is tightly adhered on the surface of Al_2O_3(0001) substrate. **g-h,** The micrograph of the after-annealed upper surface and lower surface of Cu/Al_2O_3(0001). From the comparison, after oxidization treatment, the Cu was oxidized totally in the upper surface (dark yellow color), but no CuO_x can be seen in the lower surface except a very small area at the edge. From the enlarged image, it seems the oxidization can only happen in the non-closely adhered area, which also verified the extremely-small distance between Cu(111) and Al_2O_3(0001).

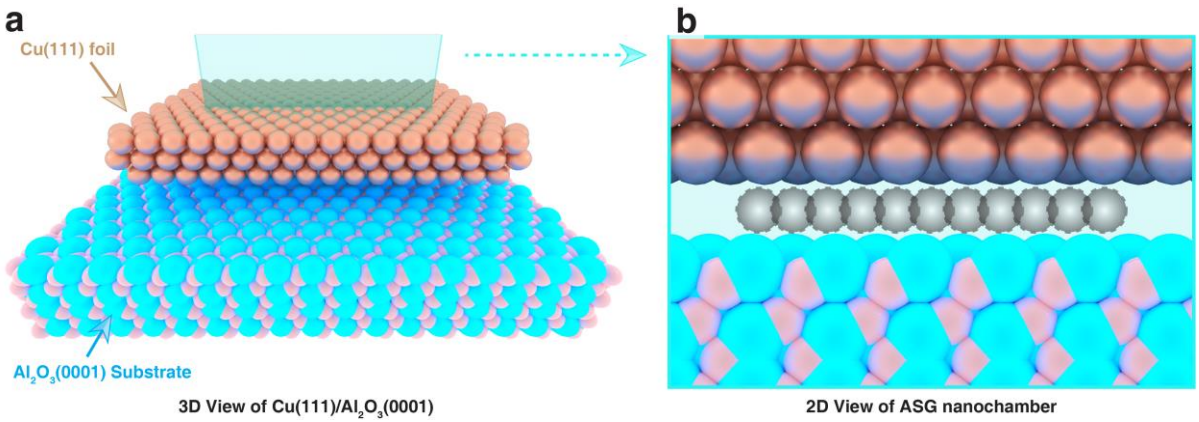

Fig. 10 | Atomic structure of the ASG nanochamber. a, 3D schematic illustration of the ASG nanochamber formed at the interface of Cu(111) and Al_2O_3(0001). **b**, 2D view of the ASG nanochamber and expected graphene formation position. According to the same lattice symmetry and good crystal mismatch between Cu(111) and Al_2O_3(0001), after the long-term annealing process, the total system will reach the lowest energy state with a smallest distance between Cu(111) and Al_2O_3(0001) with the most stable symmetry state, leading to the formation of the ASG nanochamber for the further synthesis of graphene.

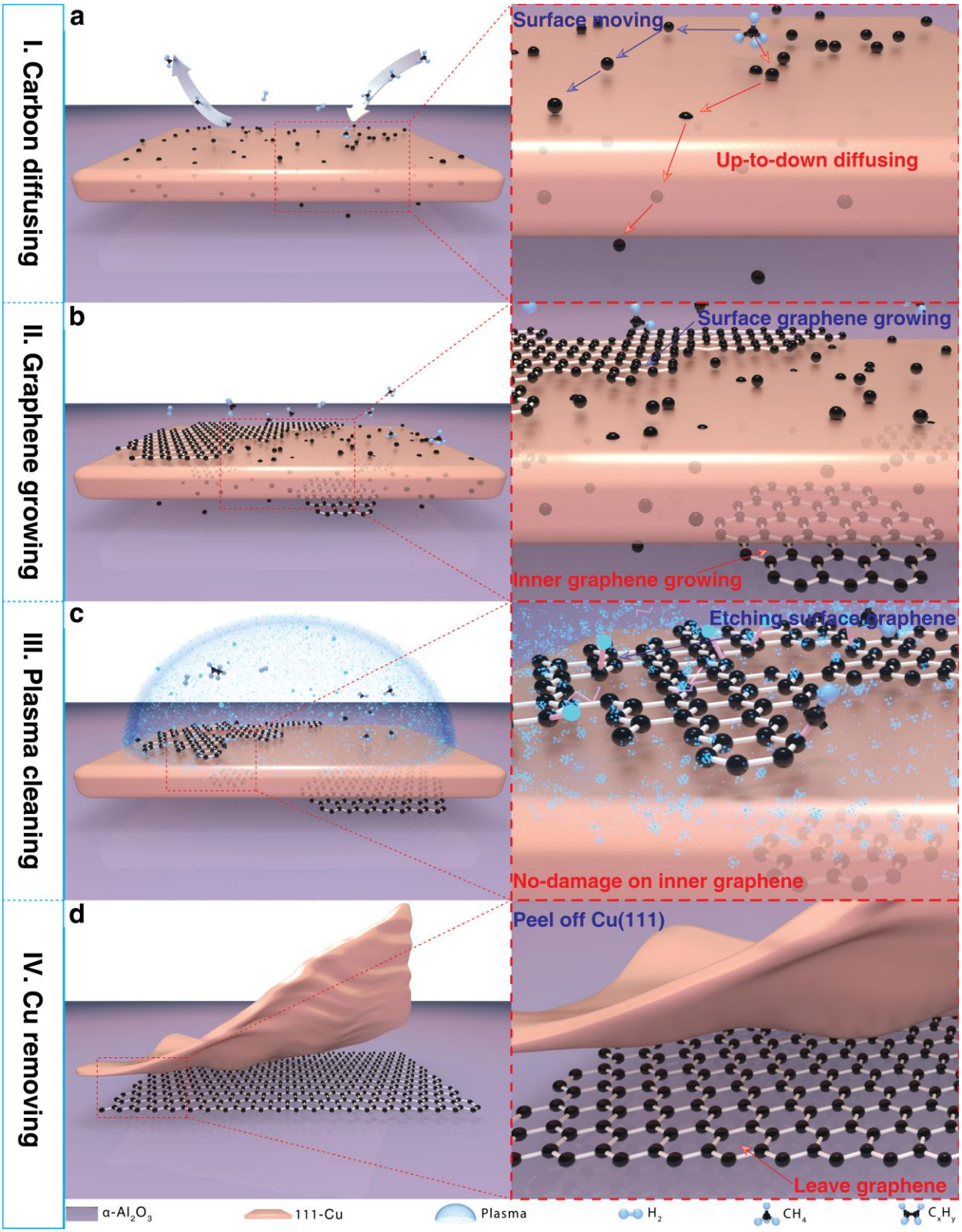
I. Carbon diffusing
II. Graphene growing
III. Plasma cleaning
IV. Cu removing
a
b
c
d
Surface moving
Up-to-down diffusing
Surface graphene growing
Inner graphene growing
Etching surface graphene
No-damage on inner graphene
Peel off Cu(111)
Leave graphene
α-Al2O3
111-Cu
Plasma
H2
CH4
CxHy

Fig. 11 | Schematic of the MPE-CVD Growth Processes. a, Schematic of the carbon-diffusing process: the methane was decomposed to active carbon atoms under the catalysis of the top surface of Cu(111) foil. Some of them were moving randomly on the surface. Others dissolved into the Cu(111) foil with forming C-Cu alloy, and diffused through the foil slowly into the ASG nanochamber. Due to no grain-boundary existence in the fabricated single crystal Cu(111), the case of carbon diffusion through the grain-boundary channel will not be discussed in this experiment. **b,** Schematic of graphene growing: The active carbon atoms condensed together to form the graphene on the top surface of Cu(111) foil. Meanwhile, the diffused carbon atoms started the nucleation and epitaxy to form the graphene domains in the ASG nanochamber. Under the uniformly distributed potential and good spatial symmetry in the interface between Cu(111) and Al_2O_3(0001), the nucleus of graphene will be formed as the same crystal orientation, which results in the forming of the single-crystal graphene film after the domain merging process in the end. Moreover, due to the long-term hydrogen-gas annealing pretreatment, the carbon species in the Cu foil were removed almost totally, leading to the absence of nucleation conditions of adlayer graphene, which guarantees the monolayer film of graphene. **c,** Schematic of plasma cleaning: The formed graphene on the top surface gradually coved the Cu surface, which will prevent the Cu catalyzation and block the carbon diffusion process. Therefore, a hydrogen-argon plasma was used to remove the graphene on the top surface. (Plasma power: 200, 30-sccm H_2 and 50-sccm Ar). Under the protection of Cu(111), the graphene in the ASG nanochamber will not be damaged. By repeating the growth loop from (a) to (c), the graphene domains continuously epitaxial grew and merged to form the adlayer-free single-crystal graphene film eventually. **d,** After the growth process, the Cu(111) foil was peeled off by using the specially-designed liquid-nitrogen-assisted extreme-temperature-separation method, leaving the pure graphene on the surface of Al_2O_3(0001).

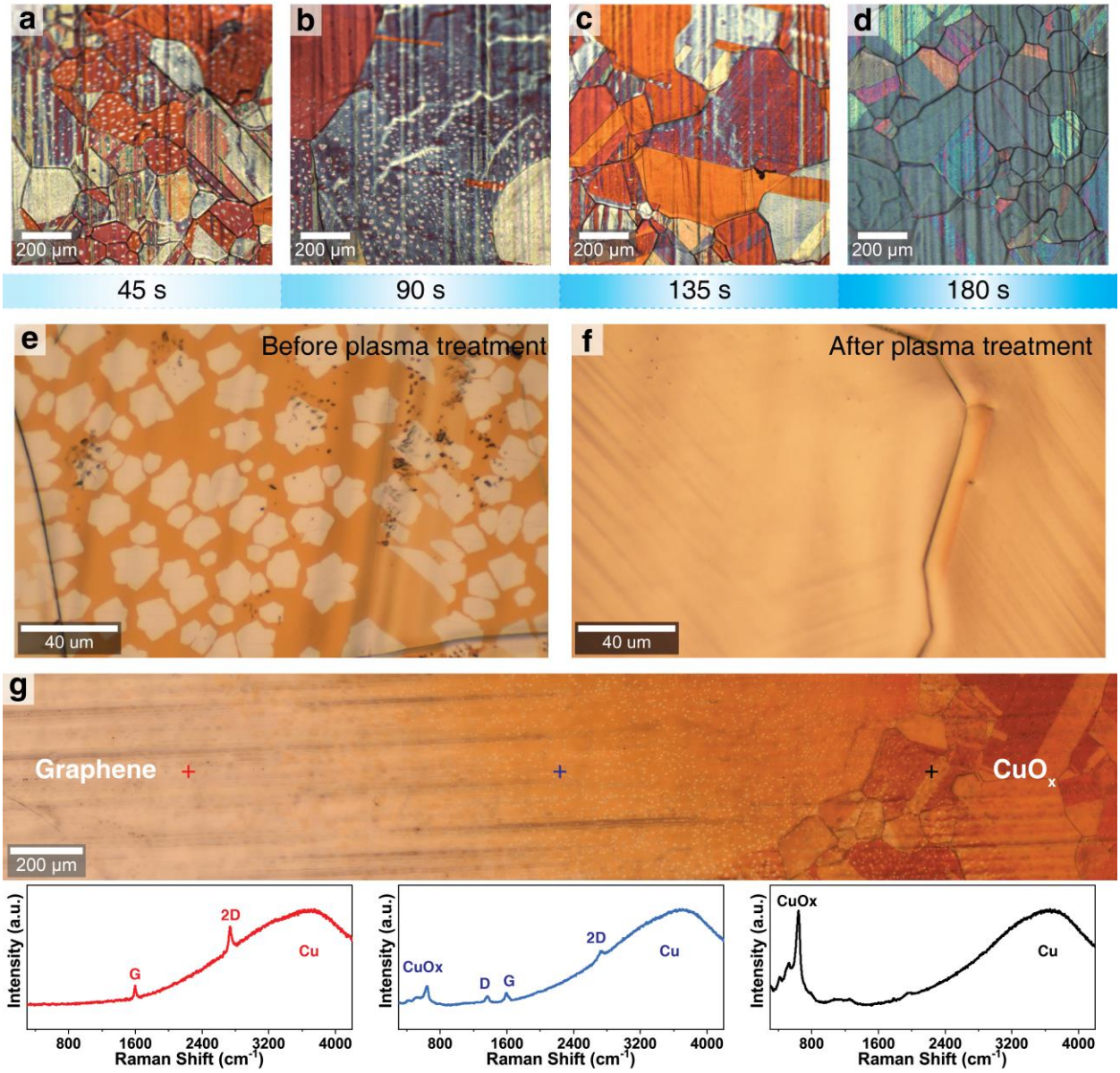

Fig. 12 | Plasma etching experiments along with various time and distance. a-d, Optical micrograph of graphene (white) distribution along the plasma treatment time. The Cu foil was oxidized for higher contrast to observe. **e-f,** Comparison of the conversional Cu-substrate graphene sample before plasma treatment and after 3-min plasma treatment. The graphene has been totally removed, as shown in (f). **g,** Optical micrograph of graphene (white) distribution along with the distance to the center of the plasma unit after 1-minute plasma treatment. The right edge is the center position of the plasma unit. The corresponding Raman spectra selected from (g) are shown in the insets.

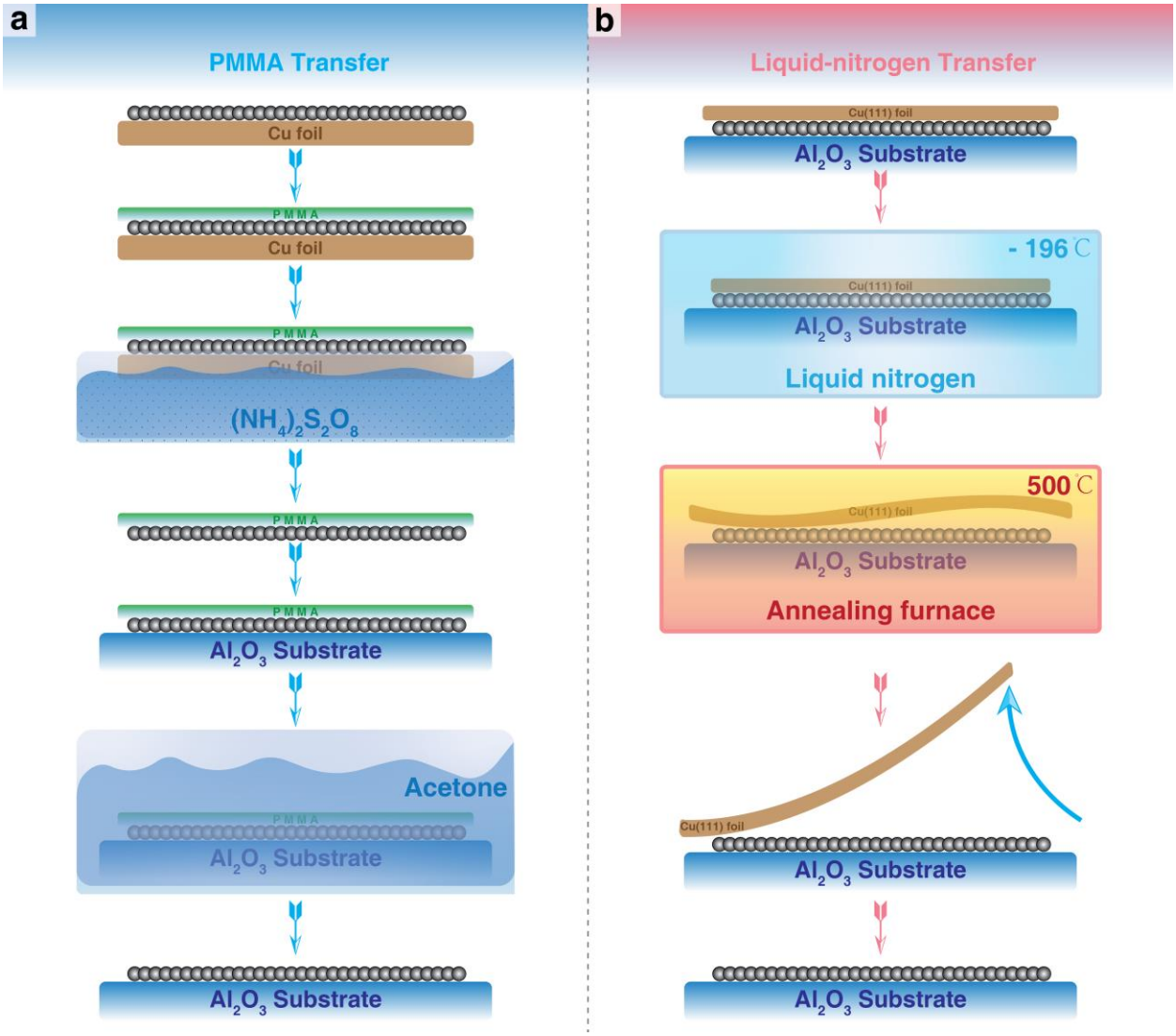

Fig. 13 | Comparison of PMMA-transfer method and liquid-nitrogen-assist separation method. a, Schematic flowchart of the conventional PMMA transfer method, which was used in the conversional graphene and h-BN transfer from Cu foil to the target substrate. **b,** Schematic flowchart of the liquid-nitrogen-assisted extreme-temperature-difference separation method. This method is specially designed for this study. The Cu(111)/graphene/Al_2O_3(0001) sample was loaded in the liquid-nitrogen cooling chamber with a temperature of -196 ℃ for 30 minutes to reach the thermally stable state. Then the sample was transferred in the hot chamber with a temperature of 500 ℃ within 3 seconds. Under the instantaneous huge temperature difference, due to the large thermal expansion coefficient of Cu foil, the relatively stable thermal deformation of sapphire, and the negative thermal expansion coefficient of graphene, the Cu(111) foil will be detached from the graphene/Al_2O_3(0001) and was peeled off physically. After that, the sample was cooling down to room temperature slowly, leaving the uncontaminated graphene on Al_2O_3(0001). The more detailed information of this transfer method will be discussed by our future work.

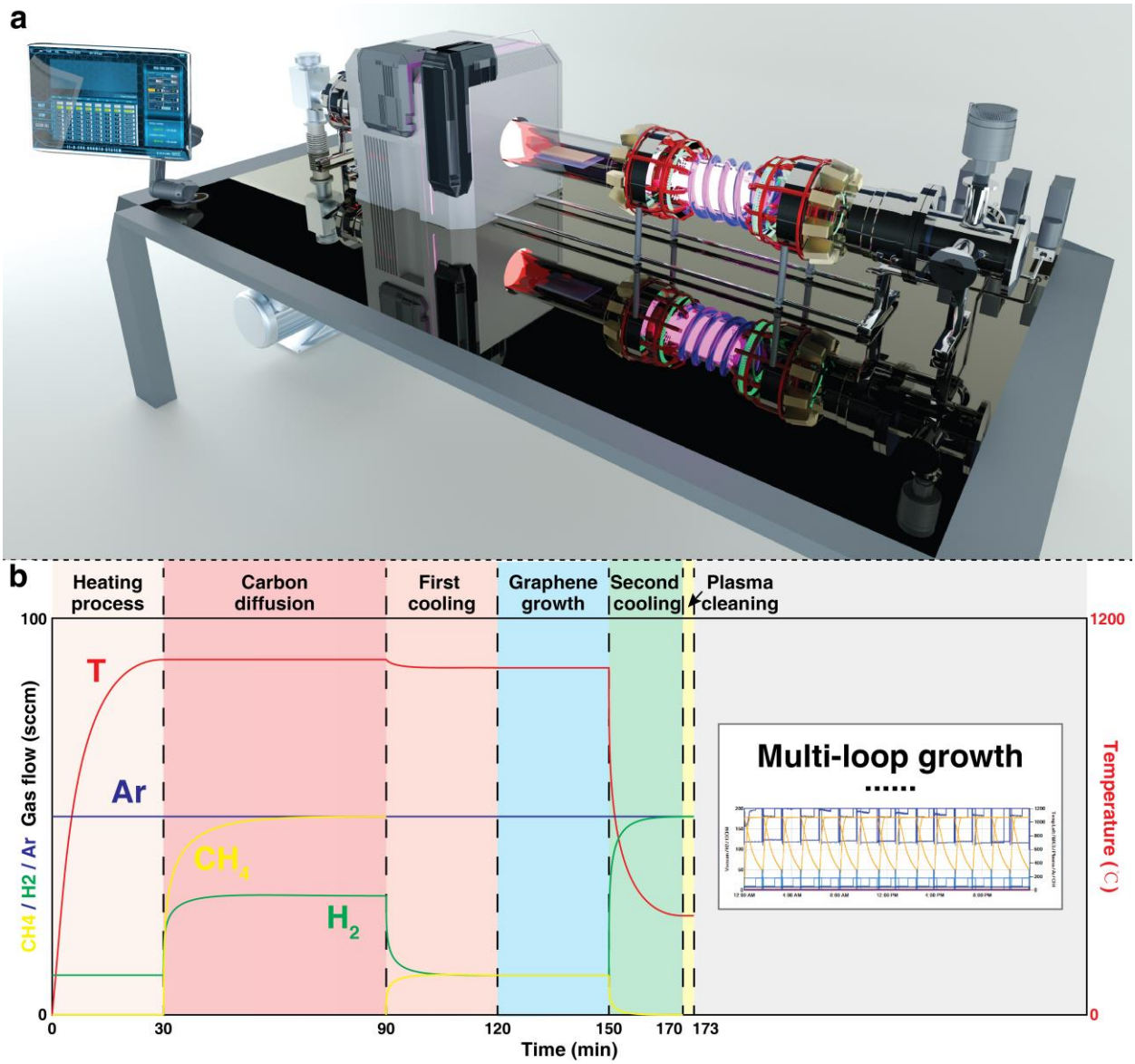

Fig. 14 | MPE-CVD growth system. a, Schematic illustration of the MPE-CVD system. This system consists of the conventional CVD system, the plasma unit, a precise pressure control system, and a computer intelligent automatic control system. **b,** Time-evolution diagram of gas flow and temperature for the MPE-CVD process for one growth loop. Inset shows the computer record of gas flow and temperature for the 15-growth-loop MPE-CVD process. Specific growth condition description: In the beginning, we loaded the long-term-annealed Cu(111)/Al_2O_3(0001) in the MPE-CVD system. Then, the system was heated to 1075 ℃ with 10-sccm H_2 and 50-sccm Ar flow under 750 Torr. After that, CH_4 with a flow rate of 50 sccm was inserted into the tube during the carbon diffusion process. 60 min later, the system was cooled to 1050 ℃ in 30 min, with the same gas mixture condition. Next, a dilute 10-sccm CH_4 gas (0.1% diluted in Ar) was purged into the system for graphene growth, with 10-sccm H_2 and 50-sccm Ar flow under 3 Torr, for 30 min. After the growth process, the system was cooled down to 300 ℃ in 20 min. Then, the CH_4 gas flow was stopped. Meanwhile, the flow of H_2 was increased to 30 sccm, and the plasma unit (200 W) was switched on for 3 min to clean the graphene surface. After that, the system was reheated to 1075 ℃ to repeat the growth loop until the whole growth process finished.

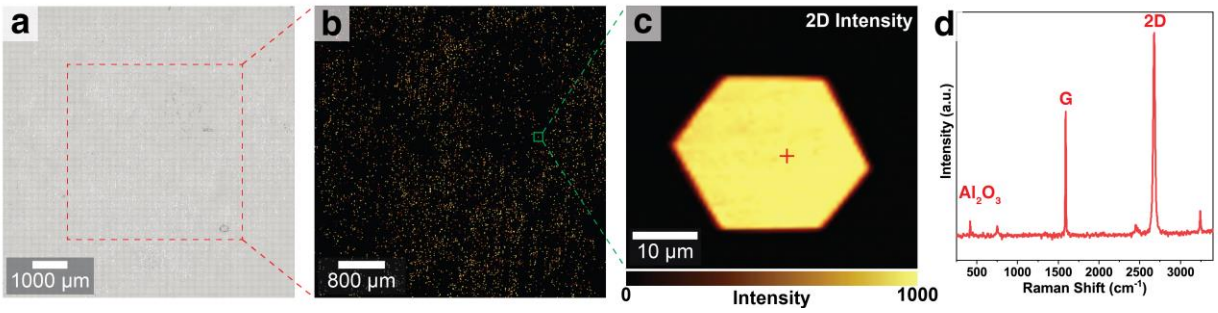

Fig. 15 | Direct-grown graphene domains on Al_2O_3(0001). a, Large-field optical micrograph of graphene domains directly grown on Al_2O_3(0001) substrates. The graphene domains can be seen as white dots. The uniformly distributed grid shadows in this figure are caused by the Microscope system when the images were stitching. **b,** Enlarged monochrome image of graphene domains in (a). The light dots are the as-grown graphene domains. **c,** Raman map of the 2D peak intensity of as-grown graphene domain in the region shown in (b). **d,** Raman spectra selected from the marked point in (c). The sharp G and 2D peaks indicate the high crystal quality of as-grown graphene.

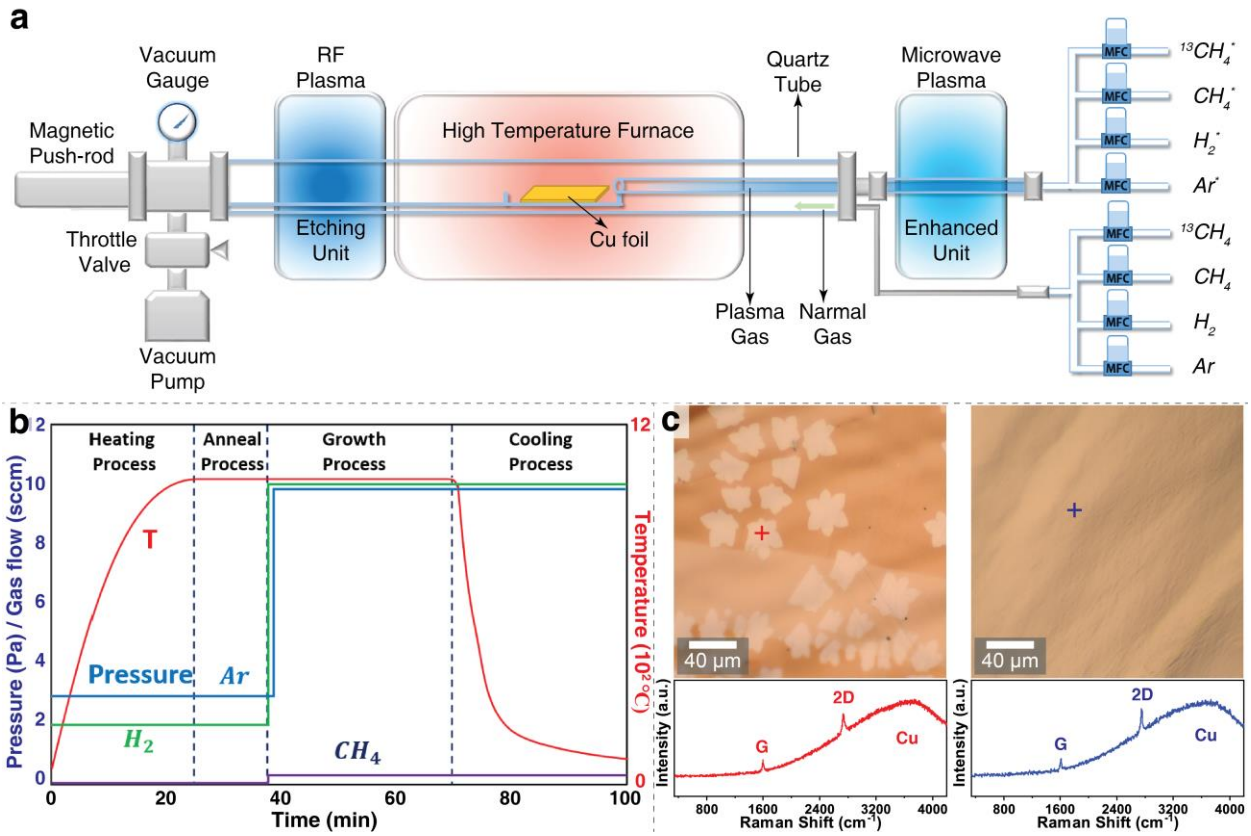

Fig. 16 | Conventional CVD growth of graphene. a, Schematic of traditional CVD growth system. **b,** Time-evolution diagram of gas flow and temperature for the CVD process. The conventional process of CVD consisted of the following three parts. (i) heating and annealing process: Cu foils were placed on a quartz boat, which was then pushed into the tube chamber. The chamber was then depressurized from 105 pa to 0.8 pa. Next, the chamber was heated up to 1030 °C by a furnace with H_2 flow; (ii) growth process: graphene grew on a Cu foil with a mixture of CH_4 and H_2 flow. (iii) cooling process: The tube chamber was cooled rapidly with the mixture gas, which was the same as that used in (ii). **c,** The Cu-substrate-grown petal-shaped graphene domain and the Raman spectra (left); and the Cu-substrate monolayer graphene film and the Raman spectra (right).

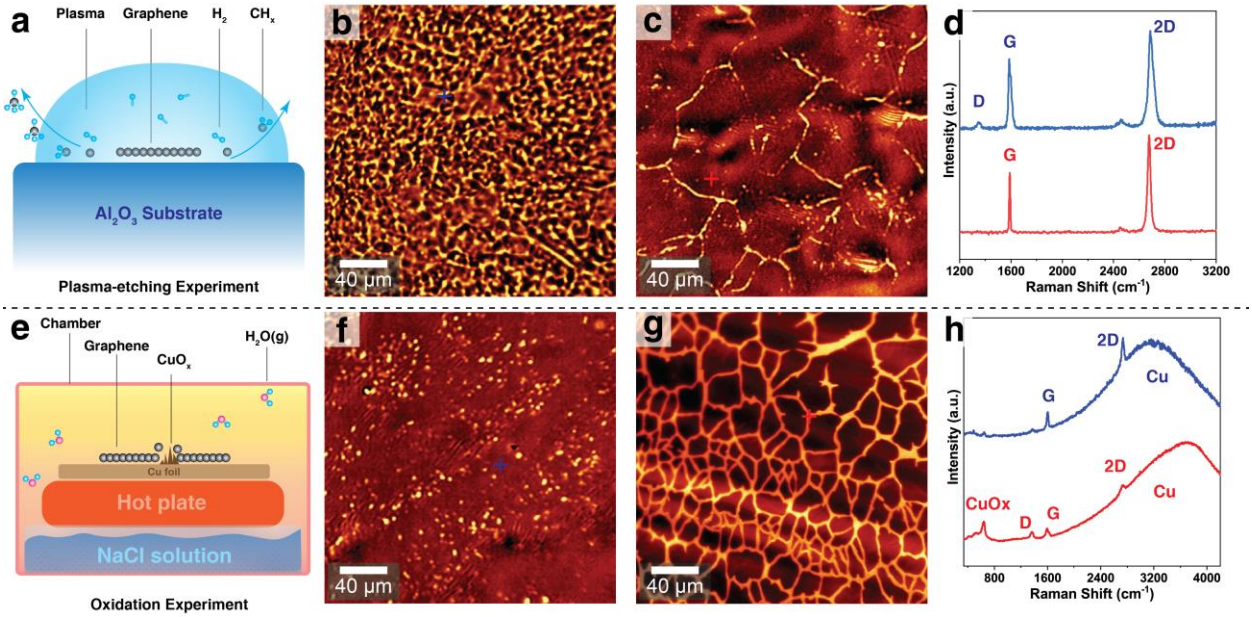

Fig. 17 | Oxygen-plasma etching and chemical-assisted grain-boundary oxidization experiments. a, Schematic illustration of the oxygen-plasma-etching experiment. **b,** The monochrome micrograph of the direct-grown graphene on the Al_2O_3 surface. Graphene was damaged uniformly by the weak oxygen-plasma. **c,** The monochrome micrograph of the transferred polycrystal graphene on the Al_2O_3 surface. The domain was damaged due to the unstable state. **d,** The Raman spectra were taken from the graphene (red) and damage areas (blue). **e,** Schematic illustration of chemical-assisted grain-boundary oxidization. The direct-grown single-crystal graphene and Cu-substrate grown polycrystal graphene were transferred to polished Cu foil. The oxidization treatment was conducted in a salt-humid environment. **f,** The monochrome micrograph of the direct-grown graphene transferred to polished Cu foil. Almost no grain boundary was observed in direct-grown single-crystal graphene. **g,** The micrograph of the Cu-substrate-grown polycrystal graphene. We observed the domain boundary circled by CuO_x in the polycrystalline graphene. **h,** The Raman spectra were taken from the no-CuO_x area (blue) and CuO_x area (red).

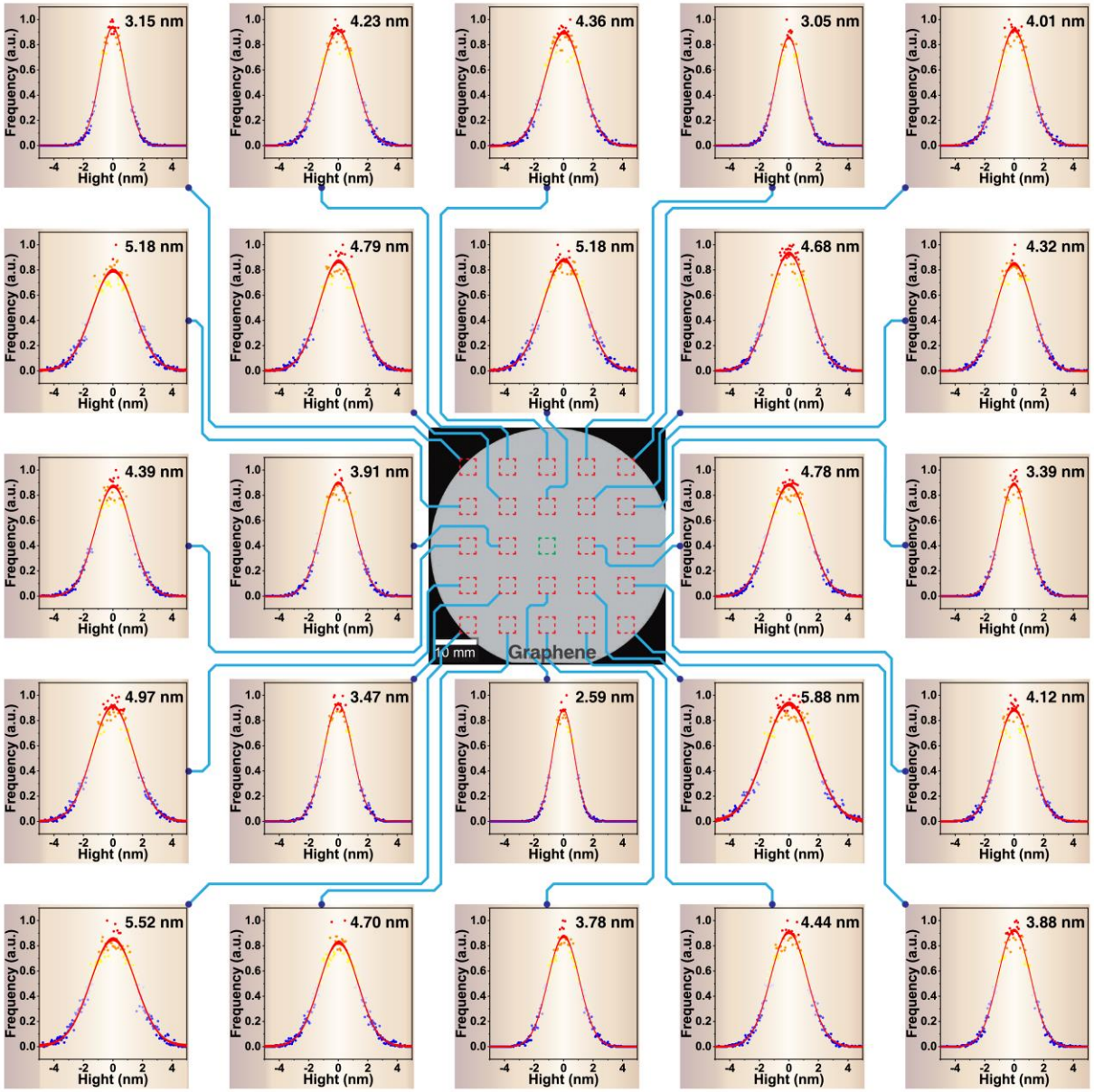

Fig. 18 | Height histograms measured by AFM from 24 selected areas (10 μm ×10 μm of each area) on as-grown graphene wafer. The AFM measurements were taken from 400 positions (20 × 20 array) of the entire graphene/Al_2O_3(0001) wafer. The surface roughness distributions are selected from 24 areas, marked by red squares on the optical micrograph, illustrating the flat surface of direct-grown graphene on Al_2O_3(0001). The average height is around 4.32 nm from the height histograms data, and most of them are lower than 6 nm.

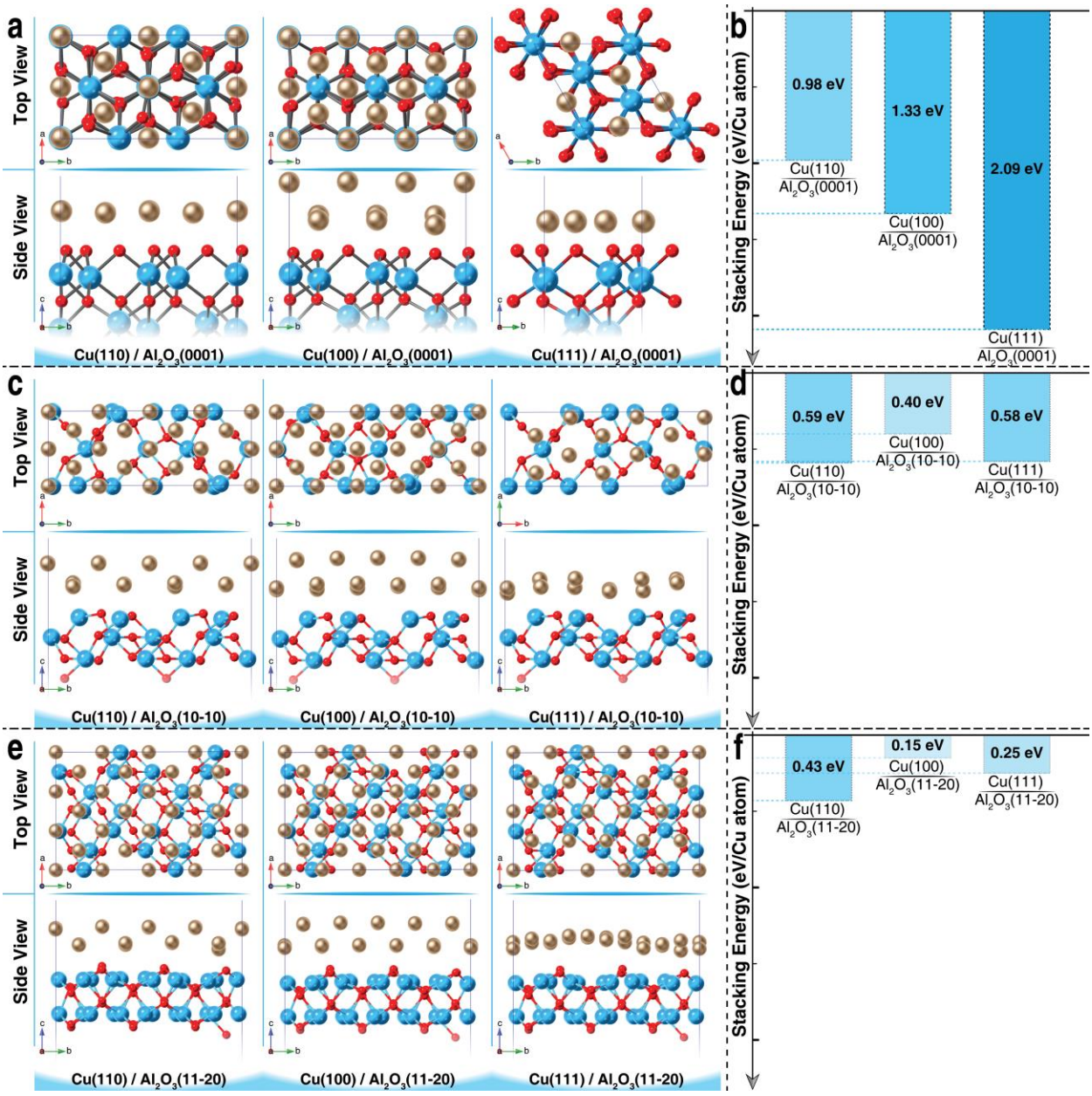

Fig. 19 | Atomic structures and DFT simulations of Cu on Al_2O_3 after relaxation. a, Top and side views of the atomic structures of Cu(110), Cu(100), and Cu(111) on Al_2O_3(0001) after relaxation. **b,** Stacking energies of Cu(100), Cu(110), and Cu(111) on Al_2O_3(0001). **c,** Top and side views of the atomic structures of Cu(110), Cu(100), and Cu(111) on Al_2O_3(10-10) after relaxation. **d,** Stacking energies of Cu(100), Cu(110), and Cu(111) on Al_2O_3(10-10). **e,** Top and side views of the atomic structures of Cu(110), Cu(100), and Cu(111) on Al_2O_3(11-20) after relaxation. **f,** Stacking energies of Cu(100), Cu(110), and Cu(111) on Al_2O_3(11-20). Cu, Al, and O atoms are shown in gold, blue, and red color, respectively.

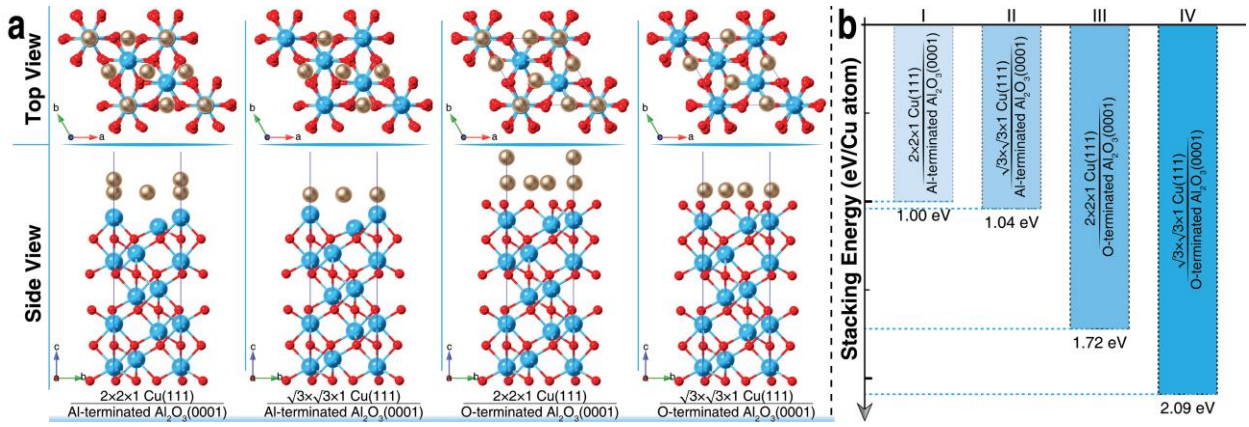

Fig. 20 | Atomic structures and DFT simulations of Cu(111) on Al-terminated and O-terminate Al_2O_3(0001). a, Comparison of the atomic structures of $2 \times 2 \times 1$ Cu(111) on Al-terminated Al_2O_3, $\sqrt{3} \times \sqrt{3} \times 1$ Cu(111) on Al-terminated Al_2O_3 $2 \times 2 \times 1$, Cu(111) on O-terminated Al_2O_3, and $\sqrt{3} \times \sqrt{3} \times 1$ Cu(111) on O-terminated Al_2O_3 after relaxation. Cu, Al, and O atoms are shown in gold, blue, and red color, respectively. **b,** Stacking energies per Cu atom in the abovementioned models.

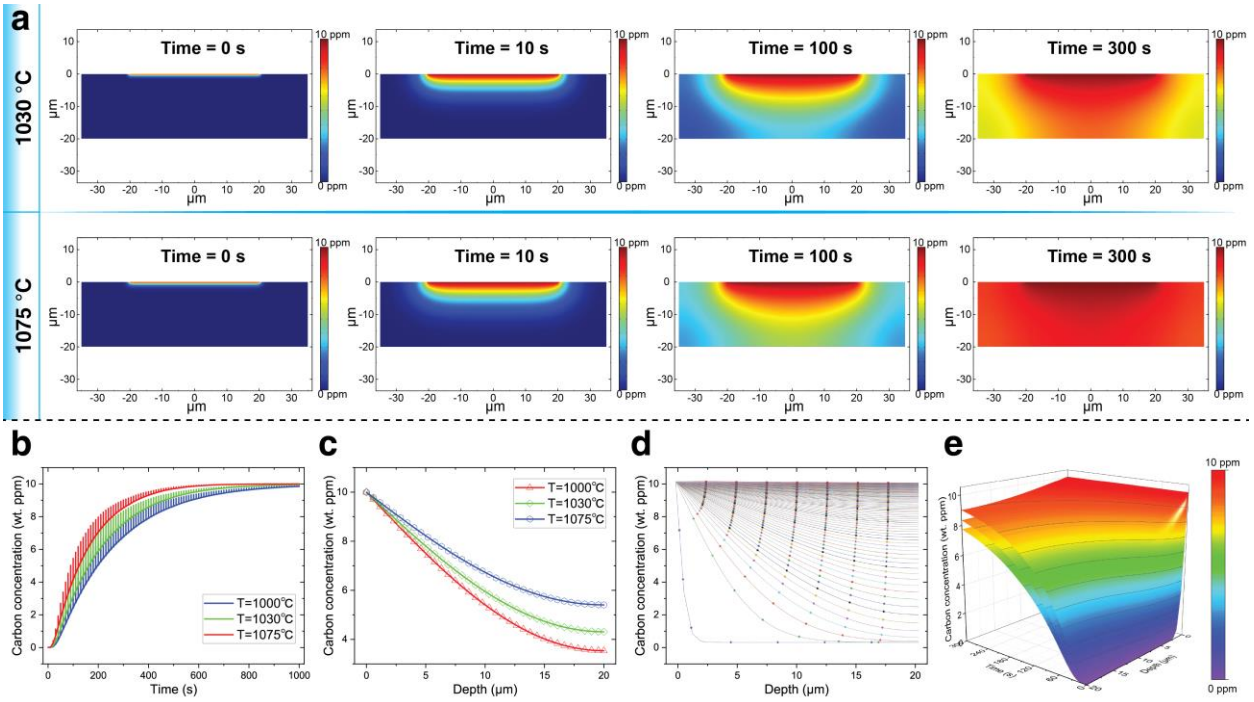

Fig. 21 | Finite element simulations of the Cu annealing process. a, Finite element simulations of the carbon-diffusion process in Cu foil (20 μm thick) at 1030 °C and 1075 °C for different diffusion times, based on Fick's laws and convection-diffusion equations. **b,** Changes of the carbon concentration in the bottom surface of the Cu foil for different diffusion times and temperatures. **c,** Distribution of the carbon concentration at different depths from the upper Cu surface after 100 s of diffusion for different temperatures. **d,** Distribution of the carbon concentration at different depths from the upper Cu surface as a function of the change of the diffusion time at 1030 °C. **e,** Carbon concentration at different depths from the upper Cu surface for different diffusion times and temperatures.

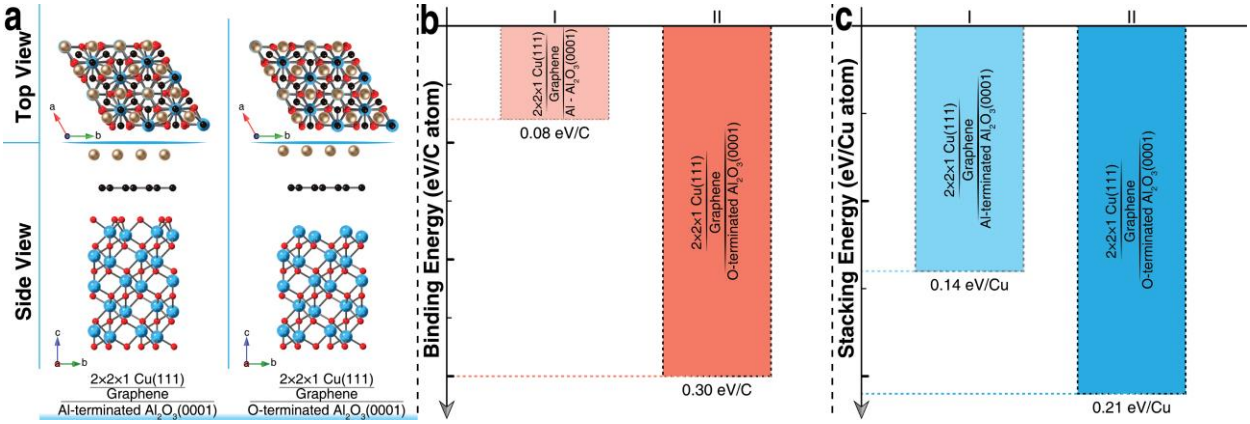

Fig. 22 | Atomic structures and DFT simulations of Cu(111) and graphene on Al-terminated and O-terminated Al_2O_3(0001). a, Comparison of the atomic structures of graphene between Cu(111) and O-terminated Al_2O_3 and of graphene between Cu(111) and Al-terminated Al_2O_3 after relaxation. Cu, Al, O, and carbon atoms are shown in gold, blue, red, and black color, respectively. **b,** Binding energies per carbon atom in the abovementioned models. **c,** Stacking energies per Cu atom in the abovementioned models.

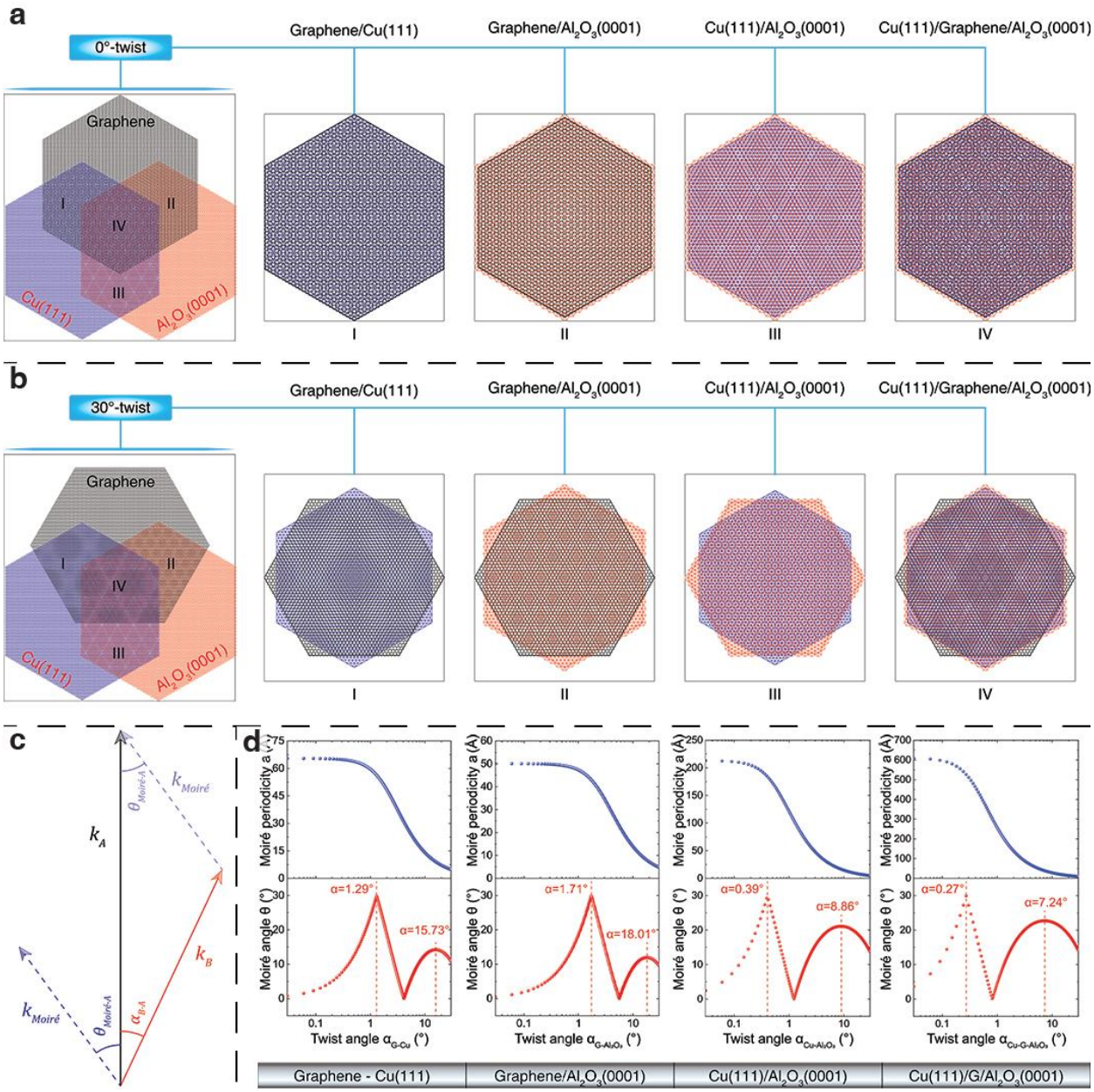

Fig. 23 | Moiré patterns of stacked graphene, Cu(111), and Al_2O_3(0001). a, Moiré patterns formed by graphene/Cu(111), graphene/Al_2O_3(0001), Cu(111)/Al_2O_3(0001), and Cu(111)/graphene/Al_2O_3(0001) with 0° and 60° twist angles. **b,** Moiré patterns formed by graphene/Cu(111), graphene/Al_2O_3(0001), Cu(111)/Al_2O_3(0001), and Cu(111)/graphene/Al_2O_3(0001) with 30° twist angle. **c,** Geometrical relationship of the Moiré reciprocal lattice vector $k_{Moiré}$ to the original reciprocal lattice vectors k_A and k_B. **d,** Changes of the Moiré periodicity and Moiré angle as functions of the twist angle between the two layers in the four combinations.

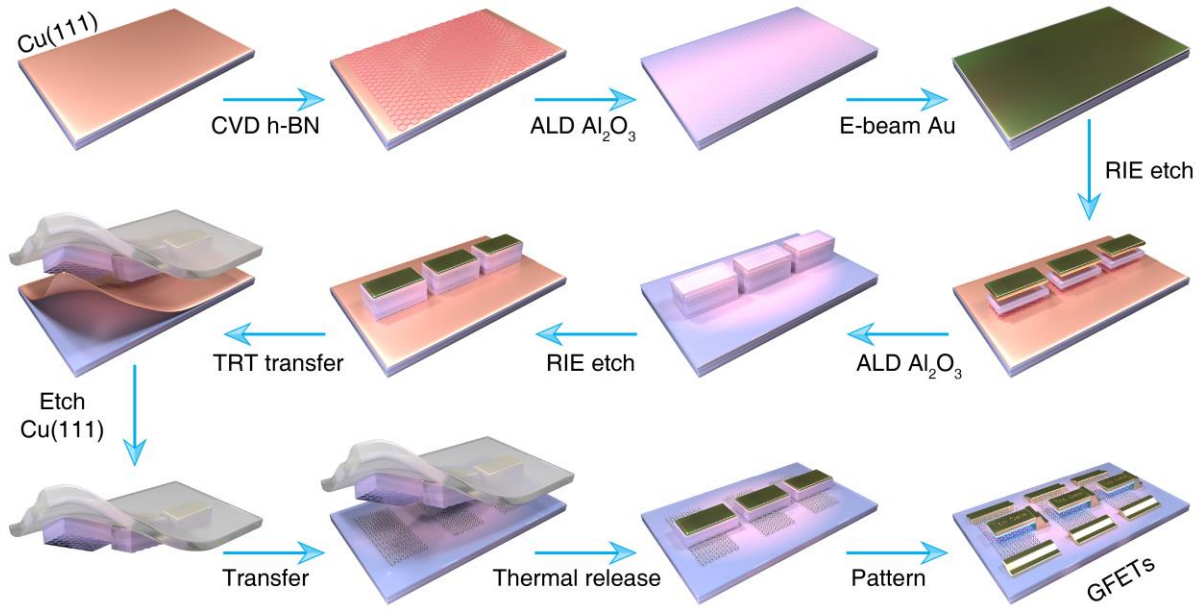

Fig. 24 | Schematic illustration of the top-gated GFETs fabrication. The top-gated GFETs were fabricated by the transferred gate stacks method. In the beginning, a 300-nm Cu film was deposited on an Al_2O_3(0001) substrate by e-beam evaporation, and then it was annealed to the fabricated Cu(111) film on this substrate. Then, the single-crystal h-BN was grown on the Cu(111) film by CVD. After that, a standard ALD was conducted of the 50-nm Al_2O_3 film. Then, a 50-nm gold film was deposited. The traditional lithography and RIE process was then used to pattern the gate stacks of Au/Al_2O_3/h-BN. Next, a thin-layer Al_2O_3 film was deposited again to form the gate sidewall by ALD. Afterward, the RIE process was used again to remove the surfaced Al_2O_3. Then, a thermal released tape was used to peel off the gate stacking, and the bottom Cu(111) film was etched. The gate stacks of Au/Al_2O_3/h-BN were then transferred onto a patterned graphene/Al_2O_3 (0001) substrate by the thermal releasing process. Finally, the source and drain electrodes were fabricated using e-beam lithography.

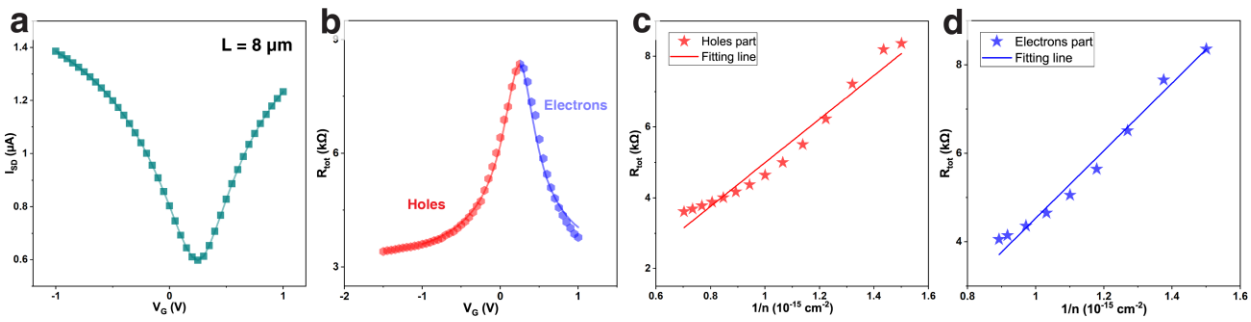

Fig. 25 | Electronic transport property measurement of GFETs. a, Typical I_{SD}-V_G characteristics measured from GFETs based on the direct-grown graphene. **b,** Fitting results of R_{tot} versus V_G using the constant mobility model. **c-d,** R_{tot} versus *1/n* curve with the linear fitting by MATLAB for holes and electrons.

Carriers transport in GFET can be described by the drift-diffusive model. According to the model, the total resistance can be obtained by

$$R_{Total} = R_{Contact} + R_{Channel}, \tag{1}$$

where $R_{Contact}$ denotes the contact resistance between source/drain electrode and graphene, and $R_{Channel}$ denotes the resistance of the graphene channel, which can be expressed by

$$R_{Channel} = \frac{L_G}{W_G} \cdot \frac{1}{e} \cdot \frac{1}{n_{Total} \cdot \mu_{carrier}}, \tag{2}$$

where e denotes the element charge, L_G and W_G denote the length and width of the graphene channel, $\mu_{carrier}$ and n_{Total} are mobility and concentration of electrons or holes. Therefore, we need to obtain the value of *n* before retrieving μ. Generally, it is impossible to give the exact value of *n* because it is calculated using analytic equations and not easy to express through analytical expressions. But especially in the GFET, the Fermi level of graphene can be assumed as identical to the Dirac level, and the energy gap is zero.

The carrier concentration can be given by

$$n_0 = \int_{E_{Dirac}}^{\infty} \rho(E) f(E) dE, \tag{3}$$

where $\rho(E)$ is the linear density of states in graphene, $f(E)$ is Fermi-Dirac distribution function, and E_{Dirac} = 0 is the reference of energy, which is chosen for convenience. The intrinsic carrier concentration can be given by

$$n_i = \frac{6}{\pi} \left(\frac{k_B T}{\hbar v_F}\right)^2, \tag{4}$$

where k_B denotes the Boltzmann constant, T is the temperature, $\hbar$ is the reduced Planck constant and $v_F = 1 \times 10^6\ m/s$ is the Fermi velocity of graphene.

The GFET behaves as a capacitor so that the total carrier concentration can be expressed approximately by

$$n_{Total} = (n_0^2 + n_{induced}^2)^{\frac{1}{2}}, \tag{5}$$

Where n_0 denotes the density of carriers at the Dirac tip, $n_{induced}$ is the induced carriers by the gate voltage. The induced carriers can be calculated by the following equation

$$n_{induced} = \frac{C}{e} \cdot \left| V_g - V_{Dirac} \right| \tag{6}$$

where *C* denotes the capacitance of 50 nm Al_2O_3 and V_{Dirac} is the value of gate voltage when $E_F = E_{Dirac}$.

According to the above equations, the total resistance can be expressed by

$$R_{Total} = R_{Contact} + \frac{L_G}{eW_G} \cdot \frac{1}{\mu_{carrier}} \cdot \left(\frac{1}{n_0^2 + \left(\frac{C}{e} \cdot |V_g - V_{Dirac}| \right)^2} \right)^{\frac{1}{2}} \tag{7}$$

To obtain the carrier mobilities (electrons and holes), we derive the equation (7) into two parts as:

$$R_{Total} = \begin{cases} R_{Contact} + \frac{L_G}{eW_G} \cdot \frac{1}{\mu_{hole}} \cdot \left(\frac{1}{n_0^2 + \left(\frac{C}{e} \cdot |V_g - V_{Dirac}| \right)^2} \right)^{\frac{1}{2}}, V_{th} < 0; \\ R_{Contact} + \frac{L_G}{eW_G} \cdot \frac{1}{\mu_{electron}} \cdot \left(\frac{1}{n_0^2 + \left(\frac{C}{e} \cdot |V_g - V_{Dirac}| \right)^2} \right)^{\frac{1}{2}}, V_{th} > 0; \end{cases} \tag{8}$$

Using the Nonlinear Least Squares Methods to fit the data, the carrier mobilities of electrons and holes can be calculated.

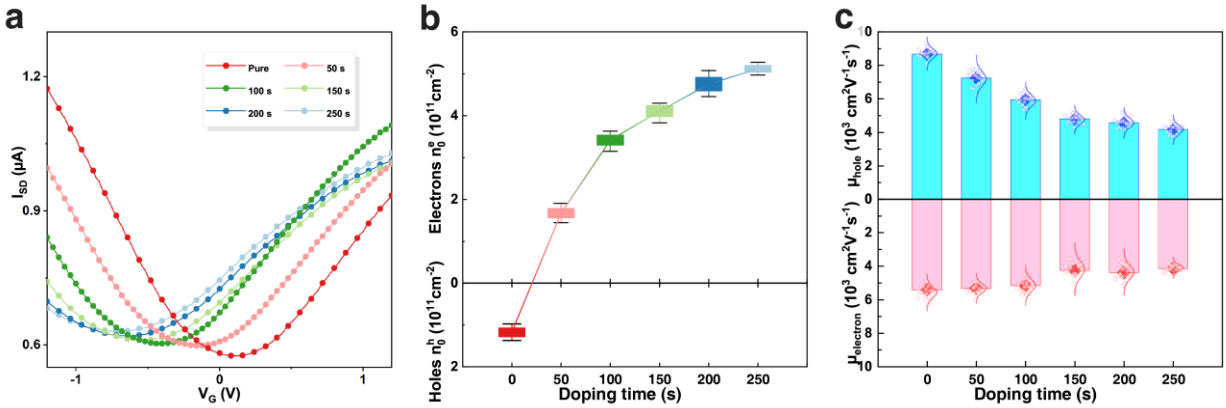

Fig. 26 | Electronic transport property measurement of GFETs from doping experiments. **a,** Typical I_{SD}-V_G characteristics measured from GFETs of direct-grown graphene with different doping times from 0 to 250 seconds. **b,** The intrinsic carrier concentration collected from 20 devices of each kind of GFET. **c,** The derived electron and hole mobility values averaged from 20 devices of each type of GFET. From the results, along with the dope time increase, the electron and hole mobilities are decreased as expected.

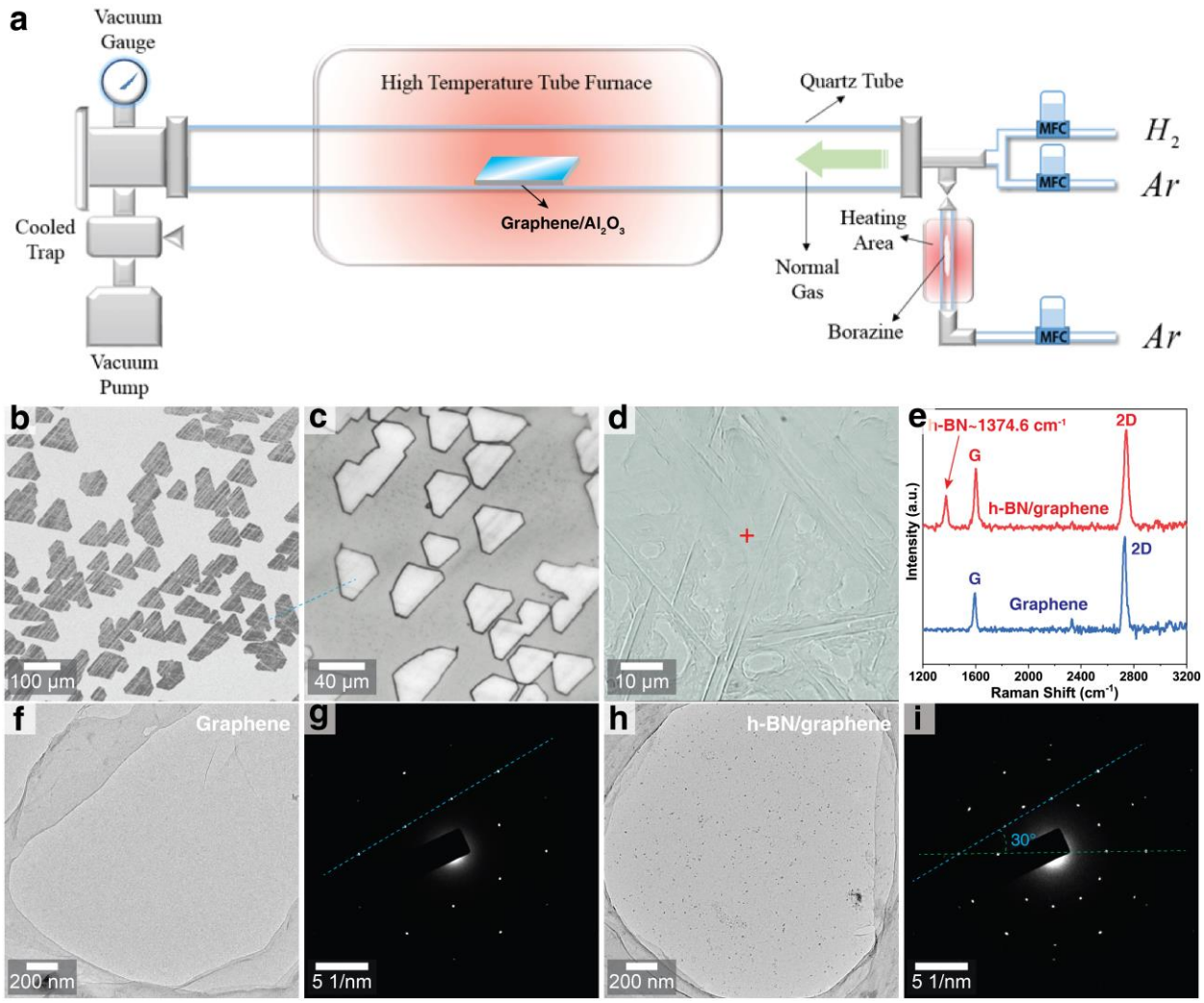

Fig. 27 | Synthesis of single-crystal h-BN on as-grown graphene/Al_2O_3(0001). a, Schematic of h-BN growth by CVD system. During the synthesis process, the borane-ammonia (97%, Aldrich) was supplied as the precursor, which was placed in a secondary chamber. The borane started to dissociate, and the products were carried into the chamber in an H_2 flow by heating the precursor to 90 °C. After growth, both the heating furnace and the heating lamp were quickly cooled down to room temperature. **b,** SEM image of as-grown aligned h-BN domains on graphene/Al_2O_3(0001) substrate. **c,** Optical micrograph of as-grown h-BN domains on graphene/Al_2O_3(0001) substrate. **d,** Optical micrograph of as-grown monolayer h-BN film on graphene/Al_2O_3(0001) substrate. **e,** Raman spectra of h-BN on graphene/Al_2O_3(0001) (red), selected from the position in (d), and the Raman spectra of graphene/Al_2O_3(0001) before growth (blue). **f-g,** TEM image of as-grown single-crystal graphene substrate and the SAED. **h-i,** TEM image of as-grown single-crystal h-BN on the graphene substrate. The SAED shows the orientation angle as 30° between h-BN and graphene.

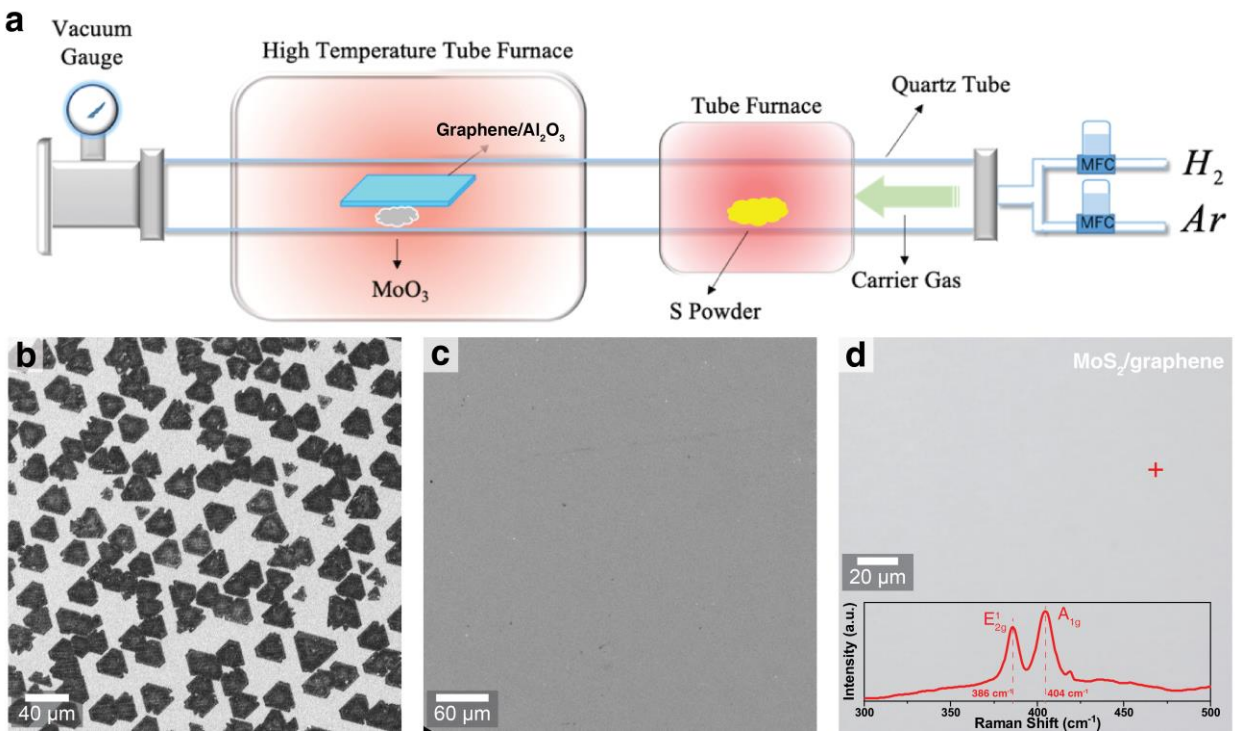

Fig. 28 | Synthesis of single-crystal MoS_2 on as-grown graphene/Al_2O_3(0001). a, Schematic of MoS_2 growth by CVD system. For MoS_2 fabrication, the MoO_3 powder and sulfur powder were supplied as the precursors. The MoO_3 powder was placed in an Al_2O_3 boat, and the graphene/Al_2O_3(0001) substrate was faced down and mounted on the top of the boat. A separate boat with sulfur powder was placed next to the MoO_3 powder. Next, the reaction chamber was heated to a growing temperature (800 °C) with a ramp rate of 50 °C min^{-1}. After growth, the heating furnace was quickly cooled down to room temperature. **b,** SEM image of as-grown aligned MoS_2 domains on graphene/Al_2O_3(0001) substrate. **c,** SEM image of as-grown monolayer MoS_2 film on graphene/Al_2O_3(0001) substrate. **d,** Optical micrograph of as-grown monolayer MoS_2 film on graphene/Al_2O_3(0001) substrate. Inset shows the Raman spectra of monolayer MoS_2 on graphene/Al_2O_3(0001).

Table 1. Stacking energies per atom obtained by DFT simulations.

System	Energy per atom
Cu(110) on O-terminated Al_2O_3(10-10)	0.59 eV
Cu(110) on O-terminated Al_2O_3(11-20)	0.43 eV
Cu(110) on O-terminated Al_2O_3(0001)	0.98 eV
Cu(100) on O-terminated Al_2O_3(10-10)	0.40 eV
Cu(100) on O-terminated Al_2O_3(11-20)	0.15 eV
Cu(100) on O-terminated Al_2O_3(0001)	1.33 eV
Cu(111) on O-terminated Al_2O_3(10-10)	0.58 eV
Cu(111) on O-terminated Al_2O_3(11-20)	0.25 eV
$\sqrt{3} \times \sqrt{3} \times 1$ Cu(111) on O-terminated Al_2O_3(0001)	2.09 eV
$2 \times 2 \times 1$ Cu(111) on O-terminated Al_2O_3(0001)	1.72 eV
$\sqrt{3} \times \sqrt{3} \times 1$ Cu(111) on Al-terminated Al_2O_3(0001)	1.04 eV
$2 \times 2 \times 1$ Cu(111) on Al-terminated Al_2O_3(0001)	1.00 eV
Cu(111) on graphene on O-terminated Al_2O_3(0001)	0.21 eV
Cu(111) on graphene on Al-terminated Al_2O_3(0001)	0.14 eV

*

Stacking energy per atom of Cu on Al_2O_3(0001) defined as:

$$E_{stacking} = -(E_{nCu+Al_2O_3(0001)} - E_{nCu} - E_{Al_2O_3(0001)})/n.$$

Stacking energy per atom of Cu on graphene on Al_2O_3(0001) defined as:

$$E_{stacking} = -(E_{nCu+graphene+Al_2O_3(0001)} - E_{nCu} - E_{graphene+Al_2O_3(0001)})/n.$$

Table 2. Binding energies per atom obtained by DFT simulations.

System	Energy per atom
Graphene on Cu(111)	0.20 eV
Graphene on O-terminated Al_2O_3(0001)	0.20 eV
Graphene on Al-terminated Al_2O_3(0001)	0.09 eV
Graphene between Cu(111) and O-terminated Al_2O_3(0001)	0.30 eV
Graphene between Cu(111) and Al-terminated Al_2O_3(0001)	0.08 eV

*

Binding energy per atom of graphene on Cu(111) defined as:

$$E_{binding} = -(E_{nC+Cu(111)} - E_{nC} - E_{Cu(111)})/n.$$

Binding energy per atom of graphene on Al_2O_3(0001) defined as:

$$E_{binding} = -(E_{nC+Al_2O_3(0001)} - E_{nC} - E_{Al_2O_3(0001)})/n.$$

Binding energy per atom of graphene between Cu(111) and Al_2O_3(0001) defined as:

$$E_{binding} = -(E_{Cu(111)+nC+Al_2O_3(0001)} - E_{Cu(111)} - E_{nC} - E_{Al_2O_3(0001)})/n.$$

Table 3. Carrier mobilities for five types of GFETs (Hole | Electron).

Device number	**Grown on Al_2O_3** (10^3 $cm^2V^{-1}s^{-1}$)		**Grown on Cu** (10^3 $cm^2V^{-1}s^{-1}$)		**With wrinkle** (10^3 $cm^2V^{-1}s^{-1}$)		**With adlayer** (10^3 $cm^2V^{-1}s^{-1}$)		**Exfoliated** (10^3 $cm^2V^{-1}s^{-1}$)	
#1	9.0	6.7	6.7	5.7	7.1	4.0	5.8	4.3	9.4	9.8
#2	9.8	6.7	5.7	4.5	4.6	5.1	5.6	5.2	8.6	11.8
#3	9.9	6.8	5.6	5.2	5.2	5.7	3.8	3.8	8.3	9.5
#4	10.8	6.0	5.7	4.6	6.2	3.6	3.8	4.6	8.9	9.8
#5	10.0	6.7	5.8	4.6	4.2	3.3	4.5	5.8	8.9	11.6
#6	8.4	6.9	6.0	6.1	5.0	2.7	5.7	4.0	7.2	9.1
#7	10.7	6.2	6.9	5.4	4.9	4.8	5.3	3.8	8.3	10.8
#8	9.9	5.2	5.6	5.3	5.5	3.1	4.0	4.7	9.8	9.2
#9	8.9	5.8	7.4	5.8	4.1	5.3	5.3	3.8	8.4	11.3
#10	9.7	5.8	5.6	4.9	6.2	3.5	5.3	4.8	10.6	10.2
#11	9.9	5.6	6.5	5.3	7.2	3.2	5.1	5.2	8.4	10.1
#12	10.2	6.2	7.5	5.4	5.2	4.8	6.0	4.1	8.6	9.7
#13	10.4	7.4	7.6	5.6	5.5	5.6	6.3	5.0	8.6	10.5
#14	9.3	5.9	5.8	4.7	5.9	3.1	7.9	5.0	8.3	11.3
#15	9.8	6.0	4.7	4.2	6.7	3.3	5.8	5.3	9.1	8.8
#16	10.0	5.3	6.7	6.0	6.0	3.6	5.2	5.3	9.0	9.2
#17	9.2	7.0	4.5	6.1	6.1	2.9	4.9	2.7	8.8	10.5
#18	10.9	7.1	5.1	4.9	5.6	4.4	5.2	3.7	9.1	9.3
#19	9.9	5.4	6.5	6.1	5.5	5.6	5.8	4.7	9.4	9.8
#20	10.0	7.3	6.9	4.4	5.9	4.2	4.2	3.6	8.6	8.7
Average	*9.8*	*6.3*	*6.1*	*5.2*	*5.6*	*4.1*	*5.3*	*4.5*	*8.8*	*10.0*

Table 4. Summary of carrier mobilities of CVD graphene-based FET reported in the literature.

Substrate	Growth temp. (℃)	Layer number	Crystallinity	Domain size (μm)	Feature	Mobility ($cm^2 V^{-1} s^{-1}$)	Ref.
Cu	1030	Monolayer	Polycrystalline	0.1−1000	N.A.	4050−6500	[1-3]
✲	1050	Monolayer	Single-crystal	10.0−50.0	Adlayer-free Wrinkle-free	11000	[4]
Glass	160−1000	Few-layer	Polycrystalline	0.04−0.05	N.A.	667−1800	[5-7]
✲	1100	Few-layer	Polycrystalline	N.A.	N.A.	4820	[8]
SiO_2/Si	600−1050	Few-layer	Polycrystalline	0.38−10.0	N.A.	43−672	[9-11]
✲	1130	Monolayer	Polycrystalline	0.20-0.50	Wrinkle-free	4000	[12]
Al_2O_3	400−1100	Few-layer	Polycrystalline	N.A.	N.A.	100−1600	[13-15]
✲	1500	Few-layer	Polycrystalline	0.03−0.27	N.A.	3000	[16]
Al_2O_3(0001)	***1050***	***Monolayer***	***Single-crystal***	**10.0−30.0**	**Adlayer-free Wrinkle-free**	**10900**	***This work***

*

Data were selected from common values (first line) and the superior values (second line "✲") for each type of growth substrate, based on the literature survey.
The performance of all G-FET was measured at room temperature.

Table 5. Intrinsic hole concentrations for five types of GFETs.

Device number	**Grown on Al_2O_3** (10^{11} cm^{-2})	**Grown on Cu** (10^{11} cm^{-2})	**With wrinkle** (10^{11} cm^{-2})	**With adlayer** (10^{11} cm^{-2})	**Exfoliated** (10^{11} cm^{-2})
#1	0.9	0.9	1.6	1.0	1.3
#2	0.6	1.1	1.1	1.2	2.0
#3	0.3	1.3	1.9	1.7	1.3
#4	0.8	1.0	1.3	1.4	1.7
#5	1.1	1.1	2.2	1.8	2.1
#6	1.0	1.4	2.4	1.1	1.1
#7	1.0	1.2	2.1	2.1	1.8
#8	0.9	1.1	1.0	1.6	1.9
#9	0.9	1.1	1.2	1.9	1.6
#10	0.4	1.3	1.0	1.3	2.0
#11	0.8	0.7	1.9	1.5	2.0
#12	0.5	1.1	2.8	1.6	2.4
#13	0.9	1.5	2.0	1.5	3.0
#14	0.9	1.1	1.2	1.0	2.6
#15	0.5	1.3	1.8	1.2	2.8
#16	1.0	0.9	1.0	1.1	1.6
#17	0.8	1.0	1.2	1.1	2.2
#18	0.7	1.3	1.5	1.3	1.1
#19	0.9	1.0	1.3	1.3	2.0
#20	0.9	1.4	1.8	0.9	2.4
Average	*0.8*	*1.1*	*1.6*	*1.4*	*2.0*

Table 6. Carrier concentrations of GFETs for various doping times.

Device number	**Pure** (10^{11} cm^{-2})	**50 s** (10^{11} cm^{-2})	**100 s** (10^{11} cm^{-2})	**150 s** (10^{11} cm^{-2})	**200 s** (10^{11} cm^{-2})	**250 s** (10^{11} cm^{-2})
Type	Hole	Electron	Electron	Electron	Electron	Electron
#1	1.2	1.6	3.4	4.2	4.8	5.2
#2	1.2	1.4	3.3	4.3	4.5	5.1
#3	1.1	1.8	3.6	4.1	4.5	5.2
#4	1.2	1.5	3.4	4.1	4.7	5.1
#5	1.3	1.8	3.3	4.2	4.5	5.1
#6	1.2	1.7	3.4	3.9	4.8	5.1
#7	1.2	1.9	3.4	4.2	4.9	5.2
#8	1.3	1.6	3.5	4.2	4.7	5.1
#9	1.1	1.6	3.5	4.1	4.9	5.0
#10	1.1	1.7	3.2	4.2	4.8	5.1
#11	1.0	1.7	3.5	4.2	4.6	5.1
#12	1.1	1.7	3.5	4.1	4.7	5.3
#13	1.2	1.7	3.4	3.8	5.0	5.1
#14	1.2	1.6	3.6	4.2	5.1	5.1
#15	1.4	1.8	3.4	3.8	4.9	5.0
#16	1.1	1.5	3.3	4.0	4.6	5.1
#17	1.1	1.6	3.1	4.2	4.9	5.2
#18	1.0	1.8	3.4	3.9	4.8	5.1
#19	1.4	1.7	3.5	4.0	4.7	5.2
#20	1.3	1.7	3.5	4.3	4.6	5.0
Average	*1.2*	*1.7*	*3.4*	*4.1*	*4.8*	*5.1*

Table 7. Carrier mobilities of GFETs for various doping times (Hole | Electron).

Device number	**Pure** (10^3 $cm^2V^{-1}s^{-1}$)		**50 s** (10^3 $cm^2V^{-1}s^{-1}$)		**100 s** (10^3 $cm^2V^{-1}s^{-1}$)		**150 s** (10^3 $cm^2V^{-1}s^{-1}$)		**200 s** (10^3 $cm^2V^{-1}s^{-1}$)		**250 s** (10^{11} cm^{-2})	
#1	8.5	5.6	7.6	5.1	5.5	5.7	5.0	5.5	4.6	4.1	4.3	4.0
#2	8.7	5.7	7.3	5.2	5.8	5.1	4.9	4.5	4.7	4.2	4.5	4.1
#3	8.7	4.9	7.4	5.5	6.0	5.2	5.2	4.5	4.2	3.9	3.8	4.5
#4	8.6	5.8	7.8	5.6	6.0	5.5	4.6	3.7	4.3	5.1	4.3	4.2
#5	8.8	5.5	7.7	5.3	6.0	5.0	4.9	3.9	4.5	5.0	3.8	4.0
#6	8.0	5.2	7.2	5.3	6.3	5.3	5.2	3.9	4.6	4.6	4.5	4.2
#7	8.7	5.4	7.1	5.0	5.7	5.4	4.9	4.5	5.2	3.8	4.1	4.2
#8	9.0	5.4	7.1	5.4	6.0	5.2	4.6	4.0	4.6	4.3	4.7	3.9
#9	8.7	6.3	7.8	5.5	5.5	5.4	4.6	4.1	5.2	4.4	4.2	4.1
#10	8.8	6.0	6.8	6.0	6.3	4.8	4.8	3.6	4.6	4.6	4.4	4.1
#11	8.5	5.2	7.4	5.0	5.9	4.5	4.3	4.2	5.0	3.9	4.1	4.1
#12	8.8	6.0	6.6	5.4	5.7	5.1	4.8	3.9	4.6	3.6	3.8	4.4
#13	8.9	5.4	7.6	4.9	5.8	5.5	4.5	3.6	4.5	3.9	4.0	3.8
#14	8.7	5.3	7.7	5.1	5.3	5.7	4.6	4.3	4.3	4.5	4.3	3.9
#15	8.6	5.2	6.9	5.2	6.2	5.1	4.8	4.6	4.3	4.5	4.2	3.9
#16	8.5	5.5	7.1	5.6	5.7	5.2	4.5	4.2	4.6	4.7	3.9	3.8
#17	9.1	5.4	6.3	4.9	6.6	5.3	4.5	3.5	4.3	4.6	3.9	4.1
#18	8.1	5.7	7.4	5.5	6.4	4.3	5.0	5.0	4.5	4.5	4.3	3.7
#19	9.4	5.9	6.7	5.2	5.3	5.0	4.3	4.3	4.7	4.2	3.8	4.4
#20	8.8	5.5	6.6	5.6	6.0	4.5	5.2	4.0	4.2	4.8	4.3	4.2
Average	*8.7*	*5.6*	*7.2*	*5.3*	*5.9*	*5.1*	*4.8*	*4.2*	*4.6*	*4.3*	*4.2*	*4.1*

Movie 1. Schematic animation of direct growth of single-crystal graphene on insulating substrates by MPE-CVD. This movie contains the (i) single-crystal Cu(111) production, (ii) graphene growth process in the MPE-CVD system: carbon-diffusing process, graphene growing process, hydrogen-argon plasma cleaning process, and Cu separation process, and (iii) top-gate GFET fabrication.

Discussion of the difference of published work by Su, et al. with this study.

Comparison Table		
Study / Point	***Nano Lett. 11, 3612-3616 (2011)***	***Our Study***
Title	***Direct Formation of Wafer Scale Graphene Thin Layers on Insulating Substrates by Chemical Vapor Deposition***	***Wafer-Scale Single-Crystal Monolayer Graphene Grown Directly on Insulating Substrates***
Main Work	This study reported the synthesis of wafer-scale graphene thin layers on the surface of SiO2 by the conventional CVD method. The key idea is to deposit a thin Cu film (300 nm) on the SiO_2 or quartz to form the sandwich structure. Then, the methane gas diffused through the Cu grain-boundary channels to the interface, decomposed, and formed graphene layers. The graphene can be left on the surface of the SiO_2 or quartz after etching the upper-layered Cu film.	This study achieved the wafer-scale adlayer-free wrinkle-free single-crystal monolayer graphene in the interface of highly-interacted Cu(111)-Al_2O_3(0001) by MPE-CVD. The primary process is fabricating the single-crystal Cu(111) foils (20 um) on Al_2O_3(0001), leading to the formation of an atomic-scale thick growth nanochamber with graphene-matched uniform-distributed lattice potential. Then, by utilizing the carbon dissolution in the Cu(111) to form C-Cu allow, diffusion into the nanochamber to form single-crystal graphene on the sapphire surface.
Substrate Structures	**Deposited Polycrystalline Cu film/SiO_2** o <u>The Cu is deposited as a thin film with a thickness of ~ 300 nm</u> o Weak interaction with insulating substrates; o Easier to evaporate under a high temperature, limiting the growth and annealing time of CVD growth. ➢ <u>The Cu is polycrystalline</u> o The crystal quality of deposited Cu is not good as as-received Cu foil; o Many grain boundaries, crystal dislocations, and lattice defects exist in the Cu film. o Different crystal symmetries and surface lattice parameters of various Cu crystal domains, leading to the polycrystalline graphene formation. ➢ <u>The considerable distance between deposited Cu film and SiO_2</u> o The considerable gap distance of Cu and SiO_2 allow that methane can diffuse from grain boundaries and even edges of Cu film to the internal area to grow graphene; o Weak interaction results in that graphene layers preferentially formed on the bottom surface of Cu film. o The graphene layers grew as the conventional CVD growth on Cu so that the wrinkles can be formed during the cooling process. ➢ <u>No lattice matching between Cu and insulating substrates</u> o According to the amorphous structure of the selected SiO_2substrate, there is no lattice matching between the Cu film with substrates. o No mechanism to limit the nucleus of graphene to align as the same crystal orientation at the interface.	**Produced Single-crystal Cu(111) foil/Al_2O_3(0001)** ➢ <u>The annealing-formed Cu(111) foil with thickness ~ 20 um</u> o Strong interaction with Al_2O_3(0001) substrate; o More stable lattice structure and better tolerance to high temperature than the deposited Cu film. ➢ <u>The Cu(111) is single-crystal</u> o The Cu(111) foil has good crystal quality after long-term near-melting-temperature annealing; o The wafer-scale single-crystal Cu(111) does not have domain boundaries. o Uniform C_{6v} crystal symmetry and small lattice mismatch along with the whole Cu(111) area, resulting in the single-crystal graphene formation. ➢ <u>The atomic-scale distance between Cu(111) foil and Al_2O_3(0001)</u> o The Cu(111) foil is fabricated and tightly adhered on the Al_2O_3(0001) with atomic-scale distance, prevent methane entrance from the edge of Cu(111) foil to the inner area. o The narrow gap ensures the graphene formation at the interface under the coupled interaction of Cu(111) and Al_2O_3(0001). o The strong vdW interaction of graphene and Al_2O_3(0001) depressed the formation of wrinkles during the cooling process. ➢ <u>The small lattice mismatch between Cu(111) and Al_2O_3(0001)</u> o An ideal growth nanochamber with a small lattice mismatch with graphene was created by fabricating Cu(111) foil on Al_2O_3(0001). o Uniform superlattice potential at the interface ensured the same nucleus's crystal orientation to further merge to single-crystal graphene.

Growth Mechanisms	➢ The methane diffused from the crystal boundaries (like channels) into the interface to decompose into active carbon atoms and form graphene. ➢ The graphene growth mechanism is similar to conventional graphene growth on Cu. o There is no mechanism to limit the adlayers and wrinkles formation during the growth process. o The graphene is grown on the bottom surface of Cu film and leave on the SiO_2 surface after the Cu etching	➢ Methane decomposed to be carbon atoms on the top surface of Cu(111), which dissolved into the Cu(111) to form the C-Cu alloy structure, then diffused through the foil into the interface to grow graphene. ➢ The graphene growth is different from the conventional CVD growth on Cu o The interface with uniformly-distributed superlattice potential leads to the single crystallinity of graphene; o The pre-removing of carbon species ensures the adlayer-free property; o The strong vdW interaction of graphene with Al_2O_3(0001) depresses the wrinkles formation o The extremely-slow diffusion of carbon in Cu(111) crystal results in the hexagonal domain shape and better crystal quality.
Growth Results	➢ The synthesized graphene is a few-layered polycrystal film with noticeable wrinkles. ➢ The carrier mobility is measured by GFET as 672 $cm^2 V^{-1} S^{-1}$ with heavily p-doped.	➢ The as-grown graphene is an adlayer-free single-crystal monolayer without wrinkles and defects. ➢ The carrier mobility is measured by GFET as 10900 $cm^2 V^{-1} S^{-1}$ with a lightly p-dope.
Comparison	These two works choose a similar but commonly used metal-insulator sandwich structure as the sunstrate. However, it is different from the two sandwich structures (polycrystal Cu/SiO_2 & Cu(111)/Al_2O_3(0001)) due to the fabricated methods, material structures, and combination forms. Besides, the underlying growth mechanism is also different in terms of the carbon-feeding style, nucleus orientation, layer-control mechanism, and the existing position of grown graphene. Eventually, both two works realized the wafer-scale graphene on insulators: Su, et al. successfully obtained the graphene layers on SiO_2 and quartz at an earlier time; our study achieved the adlayer-free ultra-flat single-crystal graphene on sapphire.	

Reference

1 Li, X. *et al.* Large-Area Synthesis of High-Quality and Uniform Graphene Films on Copper Foils. *Science* **324**, 1312-1314 (2009).

2 Xu, X. *et al.* Ultrafast growth of single-crystal graphene assisted by a continuous oxygen supply. *Nature nanotechnology* **11**, 930-935 (2016).

3 Chen, S. *et al.* Millimeter‐size single‐crystal graphene by suppressing evaporative loss of Cu during low pressure chemical vapor deposition. *Adv. Mater.* **25**, 2062-2065 (2013).

4 Luo, D. *et al.* Adlayer-Free Large-Area Single Crystal Graphene Grown on a Cu(111) Foil. *Adv. Mater.* **1903615**, 1-13 (2019).

5 Kwak, J. *et al.* Near room-temperature synthesis of transfer-free graphene films. *Nat. Commun.* **3**, 1-7 (2012).

6 Zhuo, Q.-Q. *et al.* Transfer-free synthesis of doped and patterned graphene films. *ACS nano* **9**, 594-601 (2015).

7 Chen, X., Wu, B. & Liu, Y. Direct preparation of high quality graphene on dielectric substrates. *Chem. Soc. Rev.* **45**, 2057-2074 (2016).

8 Sun, J. *et al.* Direct chemical-vapor-deposition-fabricated, large-scale graphene glass with high carrier mobility and uniformity for touch panel applications. *ACS nano* **10**, 11136-11144 (2016).

9 Su, C. Y. *et al.* Direct formation of wafer scale graphene thin layers on insulating substrates by chemical vapor deposition. *Nano Lett.* **11**, 3612-3616 (2011).

10 Kato, T. & Hatakeyama, R. Direct growth of doping-density-controlled hexagonal graphene on SiO2 substrate by rapid-heating plasma CVD. *Acs Nano* **6**, 8508-8515 (2012).

11 Teng, P.-Y. *et al.* Remote catalyzation for direct formation of graphene layers on oxides. *Nano Lett.* **12**, 1379-1384 (2012).

12 Wang, H. *et al.* Primary Nucleation-Dominated Chemical Vapor Deposition Growth for Uniform Graphene Monolayers on Dielectric Substrate. *J. Am. Chem. Soc.* **141**, 11004-11008 (2019).

13 Wei, D. *et al.* Critical crystal growth of graphene on dielectric substrates at low temperature for electronic devices. *Angew. Chem.* **125**, 14371-14376 (2013).

14 Wei, D. *et al.* Low temperature critical growth of high quality nitrogen doped graphene on dielectrics by plasma-enhanced chemical vapor deposition. *ACS nano* **9**, 164-171 (2015).

15 Song, H. J. *et al.* Large scale metal-free synthesis of graphene on sapphire and transfer-free device fabrication. *Nanoscale* **4**, 3050-3054 (2012).

16 Fanton, M. A. *et al.* Characterization of graphene films and transistors grown on sapphire by metal-free chemical vapor deposition. *Acs Nano* **5**, 8062-8069 (2011).